ACS Catalysis

Review

pubs.acs.org/acscatalysis

Oxygen Reduction in Alkaline Media: From Mechanisms to Recent Advances of Catalysts

Xiaoming Ge,[†] Afriyanti Sumboja,[†] Delvin Wuu,[†] Tao An,[†] Bing Li,[†] F. W. Thomas Goh,[†] T. S. Andy Hor,*[,†,‡] Yun Zong,*[,†] and Zhaolin Liu*[,†]

[†]Institute of Materials Research and Engineering (IMRE), A*STAR (Agency for Science, Technology and Research), 3 Research Link, Singapore 119602, Republic of Singapore

[‡]Department of Chemistry, National University of Singapore, 3 Science Drive 3, Singapore 117543, Republic of Singapore

ABSTRACT: The oxygen reduction reaction (ORR) is an important electrode reaction for energy storage and conversion devices based on oxygen electrocatalysis. This paper introduces the thermodynamics, reaction kinetics, reaction mechanisms, and reaction pathways of ORR in aqueous alkaline media. Recent advances of the catalysts for ORR were extensively reviewed, including precious metals, nonmetal-doped carbon, carbon−transition metal hybrids, transition metal oxides with spinel and perovskite structures, and so forth. The applications of those ORR catalysts to zinc−air batteries and alkaline fuel cells were briefly introduced. A concluding remark summarizes the current status of the reaction pathways, advanced catalysts, and the future challenges of the research and development of ORR.

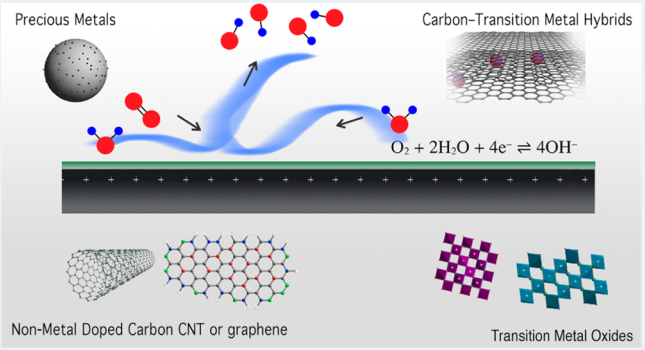

KEYWORDS: *oxygen reduction reaction, oxygen electrocatalysis, catalysts, mechanisms, reaction pathways, alkaline*

1. INTRODUCTION

Oxygen electrocatalysis is one of the most studied topics in the fields of electrochemistry and catalysis because of its importance for electrochemical energy conversion and storage devices. It deals with the oxygen electrode reactions in electrochemical systems. The oxygen reduction reaction (ORR) is the cathodic branch of oxygen electrode reactions. The ORR in aqueous solutions is highly irreversible and consists of multiple adsorption/desorption and reaction steps involving oxygen-containing species such as O, OH, O_2^-, HO_2^-, and H_2O_2.[1] Despite extensive research work over decades,[2,3] the mechanistic aspects of oxygen reduction have not been well understood because of the involvement of a net transfer of four electrons and four protons to O_2 and the cleavage of the formal double bond of O_2. Apart from the scientific significance, oxygen electrocatalysis is vitally important to the industry, largely due to the increasing demands for renewable energy technologies that rely on oxygen electrochemistry, such as metal−air batteries, fuel cells, electrocatalytic and photocatalytic water splitting, fuel synthesis, and so forth. The ORR is recognized as the kinetically limiting component of these devices based on oxygen electrochemistry. To attain high energy efficiency, it is desirable to have the oxygen electrodes of electrochemical devices to trigger the ORR as close to the reversible conditions as possible (i.e. with an overpotential as close to zero as possible). Due to the highly irreversible nature of oxygen electrode reactions, the use of electrocatalysts is of paramount importance to minimize the overpotential.

The alkaline media confers reduced adsorption energies of anions. According to the Nernst equation, the working potential of electrochemical processes in aqueous media shifts by −59 mV, equivalent to a weakening of adsorption energy of 0.059 eV for a monovalent anion, for every increase of 1 pH unit per increase. In the case of divalent anion, SO_4^{2-} adsorbs moderately on Pt in acidic media but does not adsorb to any appreciable extent on Pt in a typical ORR working potential of $0 < E < 1$ V (RHE) in strongly alkaline solutions.[4] Moreover, the alkaline nature enables surface-independent outer-sphere electron transfer processes during the first stage of ORR.[5] The surface nonspecificity sheds light on using a wide range of nonprecious metal catalysts, besides precious metals. Alkaline media provides a less corrosive environment to the catalysts, and the ORR kinetics is more rapid in alkaline media than in acidic media. A resurgence of interests on alkaline metal−air batteries,[6−8] alkaline hydrogen fuel cells,[9,10] alkaline direct alcohol fuel cells,[11,12] and microbial fuel cells[13,14] has stimulated more and more research and development on ORR catalysts in alkaline media.

We limit the scope of this review paper to ORR in aqueous alkaline media. Readers interested on ORR in acidic media are suggested to extensive review papers covering the reaction mechanisms[15−18] and electrocatalysts.[19−32] Even for ORR in

Received: March 12, 2015
Revised: June 26, 2015
Published: June 29, 2015

DOI: 10.1021/acscatal.5b00524
ACS Catal. 2015, 5, 4643−4667

alkaline media, excellent review papers and book chapters on oxygen electrocatalysis covering ORR mechanism and reaction pathways[33−35] and electrocatalysts[36] have been reported. To avoid duplicating those previous works, this review paper starts from a briefing of thermodynamics and kinetics of oxygen electrode reactions, to an overview of reaction pathways of ORR, and to recent advances (especially in the last three years) of oxygen electrocatalysts. Those oxygen electrocatalysts under review are categorized into precious metals, nonmetal-doped carbons, carbon−transition metal hybrids, and transition metal oxides, among others. A concluding remark section summarizes the research progress and outlines the future perspective.

2. THERMODYNAMICS AND KINETICS OF OXYGEN ELECTROCATALYSIS

2.1. General Principles. The standard reduction potential of O_2 to OH^-, $E^0_{O_2/OH^-}$, is 0.401 V versus Standard Hydrogen Electrode (SHE) for the direct four-electron pathway:[37]

$$O_2 + 2H_2O + 4e^- \rightleftharpoons 4OH^-;\ E^0 = 0.401\ \text{V vs SHE} \quad (1)$$

In an alternative two-electron pathway, O_2 is reduced to peroxide ion

$$O_2 + H_2O + 2e^- \rightleftharpoons HO_2^- + OH^-;\ E^0 = -0.076\ \text{V vs SHE} \quad (2)$$

followed by either further reduction

$$HO_2^- + H_2O + 2e^- \rightleftharpoons 3OH^-;\ E^0 = 0.878\ \text{V vs SHE} \quad (3a)$$

or disproportionation

$$2HO_2^- \rightleftharpoons 2OH^- + O_2 \quad (3b)$$

In acidic solutions, the four-electron (Reaction 4) and two-electron (Reactions 5, 6a, and 6b) pathways are

$$O_2 + 4H^+ + 4e^- \rightleftharpoons 2H_2O;\ E^0 = 1.229\ \text{V vs SHE} \quad (4)$$

$$O_2 + 2H^+ + 2e^- \rightleftharpoons H_2O_2;\ E^0 = 0.695\ \text{V vs SHE} \quad (5)$$

$$H_2O_2 + 2H^+ + 2e^- \rightleftharpoons 2H_2O;\ E^0 = 1.776\ \text{V vs SHE} \quad (6a)$$

$$2H_2O_2 \rightleftharpoons 2H_2O + O_2 \quad (6b)$$

In nonstandard conditions, the equilibrium potential of oxygen electrode reactions is established according to the Nernst equation:

$$E = E^0 - \frac{RT}{nF}\ln\frac{a_{Ox}}{a_{Red}} \quad (7)$$

where R is the gas constant, T is the temperature in Kelvin, n is the number of electrons transferred, F is the Faraday constant, and a is activity of the oxidized and reduced species. In the specific circumstance of alkaline media at 25 °C and at an O_2 pressure of 1 atm, $E^0_{O_2/OH^-}$ is related to the Reversible Hydrogen Electrode (RHE)

$$E_{RHE} = E_{SHE} + 0.059 \times \text{pH} \quad (8)$$

, as illustrated in Figure 1.

Considering a low solubility of O_2 of 1.26×10^{-3} mol L^{-1} in aqueous solutions, only those methods based on convective/forced transport of reactants in the solutions can enable the evaluation of ORR activity. The rotating-disk electrode (RDE) technique is a powerful tool on evaluating the activity of oxygen electrode reactions. RDE is a convective electrode system consisting of a disk of electrode and a rotating shaft (Figure 2).

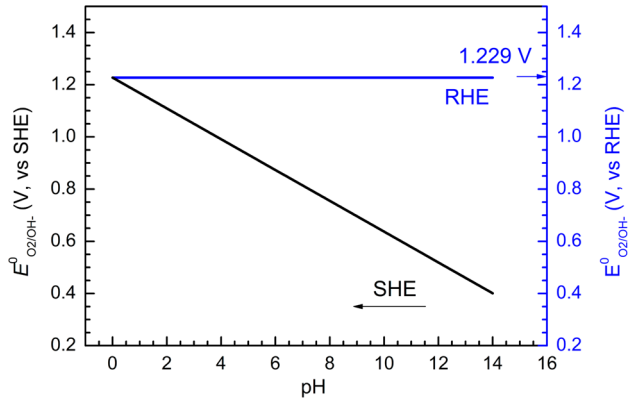

Figure 1. RHE scales with SHE of O_2/OH^- redox couple at different pH values of aqueous solutions.

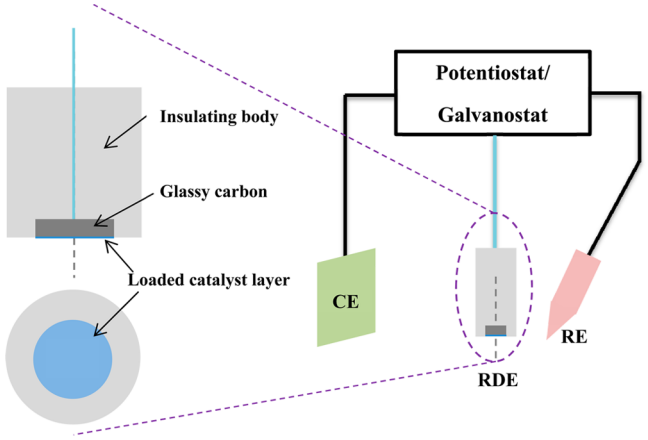

Figure 2. Schematic diagram of typical rotating-disk electrode (RDE) testing setup in three-electrode configuration. Catalysts are loaded on an embedded glassy carbon disc of RDE. CE and RE are acronyms of counter electrode and reference electrode, respectively.

Figure 3 shows a typical ORR RDE polarization curve, from which some performance indicators of reaction kinetics are

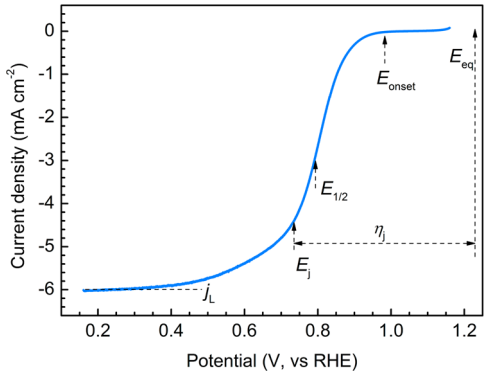

Figure 3. Typical ORR polarization curve of Pt/C collected from RDE system with rotating rate of 2000 rpm.

indicated (e.g., onset potential (E_{onset}), half-wave potential ($E_{1/2}$), overpotential under a specific current density (η_j), and diffusion-limiting current density (j_L)). The electrochemical and hydrodynamic properties of RDE is correlated with the Koutecký−Levich (K−L) equation[38]

DOI: 10.1021/acscatal.5b00524
ACS Catal. 2015, 5, 4643−4667

$$\frac{1}{j} = \frac{1}{j_L} + \frac{1}{j_K} = \frac{1}{0.62nFC_0(D_0)^{2/3}v^{-1/6}\omega^{1/2}} + \frac{1}{nFkC_0} \quad (9)$$

where j_K is the kinetic-limiting current density, ω is the angular velocity in unit of rad/s, n is the number of transferred electrons, C_0 and D_0 are the bulk concentration and diffusion coefficient of O_2 in electrolyte, v is the kinematic viscosity of the electrolyte, and k is the electron-transfer rate constant. n and k can be obtained from the slope and intercept of K–L equation, respectively.

The extent to which each of reaction pathways (1) to (6b) is involved for a particular electrocatalyst is usually established with the rotating ring-disk electrode (RRDE) technique. More than RDE that only monitors the oxygen reduction currents, RRDE has a coaxial ring electrode to detect the products generated from the disk electrode (Figure 4). The ring

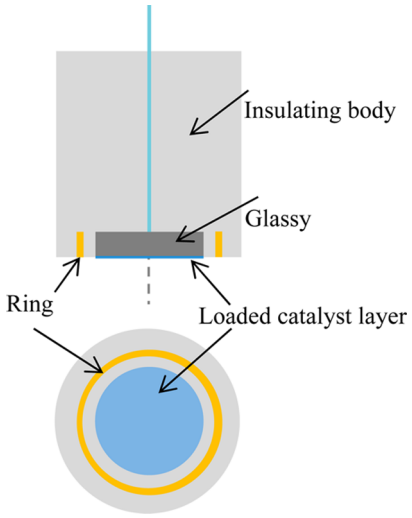

Figure 4. Schematic diagram of rotating ring-disk electrode system.

electrode is set within the potential window between the diffusion-limiting value for the oxidation of intermediates such as H_2O_2 and hydrogen peroxide anion (HO_2^-) and E_{onet} of the oxidation of OH^- to O_2. j_L of H_2O_2 oxidation on Pt RDE was attained at 0.11 V vs SCE (equivalent to 1.12 V vs RHE) in 0.1 M KOH + 0.15 M H_2O_2 solution under a rotating rate of 1000 rpm.[39] The oxidation of OH^- to give O_2 on Pt RDE emerged when the potential was larger than 0.71 V vs Ag/AgCl (equivalent to 1.69 V vs RHE) in 0.1 M KOH under a rotating rate of 2000 rpm.[40] Based on these results, a suitable potential window between 1.3–1.5 V versus RHE is recommended for the set potential of the Pt ring of RRDE. Figure 5 shows a typical RRDE curve of Pt/C.[41] The fraction of current due to HO_2^- that is recorded by the ring electrode ($X_{HO_2^-}$) and the corresponding electron transfer numbers during ORR (n_{e^-}) are[42,43]

$$X_{HO_2^-} = \frac{2I_R/N}{I_D + I_R/N} \quad (10)$$

$$n_{e^-} = \frac{4I_D}{I_D + I_R/N} \quad (11)$$

, where I_R is the ring current, I_D is the disk current, and N is the collection efficiency.

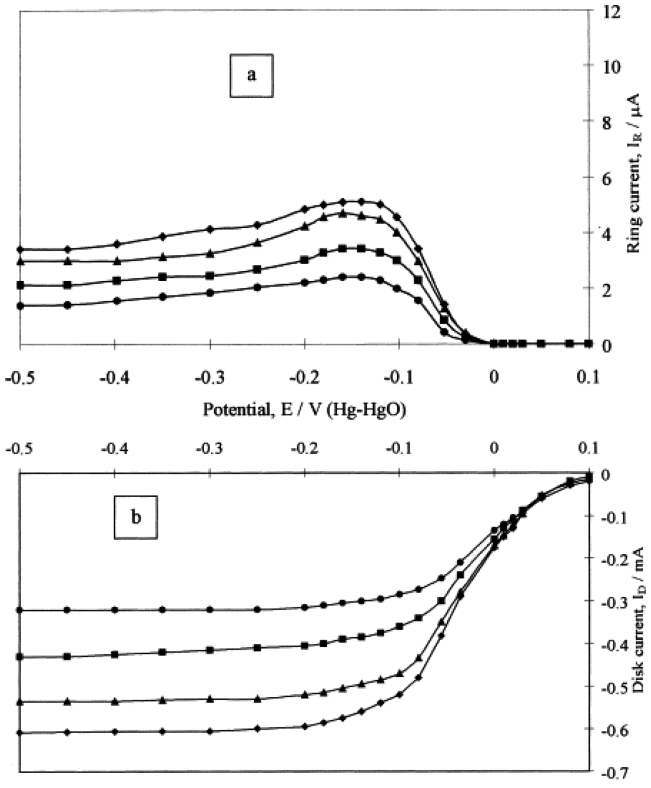

Figure 5. Current–potential curves for O_2 reduction on Pt/(Pt + C) = 20% thin layer (b) and for HO_2^- reoxidation on Pt ring electrode (a) in 1 M NaOH solution saturated with pure O_2 gas. The potential of ring current (E_R) = 0.35 V vs Hg/HgO. Rotation frequencies: (●) 500; (■) 1000; (▲) 1500; (♦) 2000 rpm. Scan rate: 1 mV s^{-1}. Reprinted with permission from ref 41. Copyright 1998 Elsevier.

At equilibrium, the η–j characteristic is described by the classic Butler–Volmer (BV) equation[38,44,45]

$$j = j_0\left[\exp\left(\frac{\alpha_a nF\eta}{RT}\right) - \exp\left(-\frac{\alpha_c nF\eta}{RT}\right)\right] \quad (12)$$

where j_0 is the exchange current density as the current density in both the cathodic and anodic directions at the equilibrium potential, α_a is the anodic charge transfer coefficient, and α_c is the cathodic charge transfer coefficient. Due to the high irreversibility nature of oxygen electrode reactions, the generated oxygen reaction currents at higher overpotentials ($|\eta|$ > 50 mV) would more appropriately be described as (by convention, the current and overpotential associated with cathodic oxygen reduction is taken as negative, and vice versa):

$$j_a = j_0\exp\left(\frac{\alpha_a nF\eta_a}{RT}\right) \quad (13)$$

$$j_c = -j_0\exp\left(-\frac{\alpha_c nF\eta_c}{RT}\right) \quad (14)$$

where the subscripts "a" and "c" denote anodic and cathodic, respectively. The Tafel equations are the semilogarithmic forms of eqs 13 and 14

$$\eta_a = \frac{RT}{nF\alpha_a}\ln j - \frac{RT}{nF\alpha_a}\ln j_0 = b\ln j - a \quad (15)$$

DOI: 10.1021/acscatal.5b00524
ACS Catal. 2015, 5, 4643–4667

$$\eta_c = \frac{RT}{nF\alpha_c}\ln j_0 - \frac{RT}{nF\alpha_a}\ln j = a - b\ln j \quad (16)$$

b is the Tafel slope, which itself is a reaction mechanism indicator as well as calculating the n value. b of −60 mV dec^{-1} corresponds to a pseudo two-electron reaction as the rate-determining step (RDS), whereas b of −120 mV dec^{-1} suggests the first-electron reduction of oxygen as RDS.[46] Note that the ORR consists of multiple steps that can each be described by j_0 and Tafel slopes. Further, because the cathodic and anodic branches of oxygen electrode reaction (i.e., ORR and OER) have RDS, the extrapolation of Tafel plot in obtaining j_0 is not valid, and j_0 should not be used as an indicator of catalytic activity of ORR.

2.2. Reaction Pathways on Precious Metals. The ORR kinetics is complicated not only because of the multiple electronic transfer steps involving four electrons but also because of the profound influences from the pH value,[47] solvation, and polarity of water.[48] Figure 6 shows the scenario

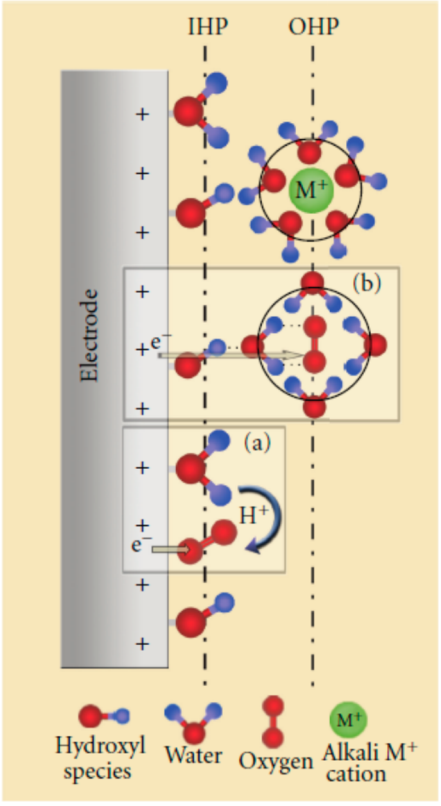

Figure 6. Double-layer structure of electrolyte/electrolyte interface during ORR in alkaline media. Insets (a) and (b) illustrate the inner- and outer-sphere electron transfer processes, respectively. IHP is the inner Helmholtz plane, and OHP is the outer Helmholtz plane. As indicated in the figure, the negative end of the water, hydroxyl species, and other intermediates orient themselves toward the positive electrode. Reprinted with permission from ref 5. Copyright 2012 Hindawi Publishing Corporation.

of double-layer structure of electrode/aqueous electrolyte interface during ORR. Inner Helmholtz plane (IHP) defines the region that is between the electrode surfaces and the IHP charged species that are closely attracted on the vicinity of electrode surfaces. In contrast, beyond the outer Helmholtz plane (OHP), the charged species are loosely scattered in the aqueous solution.[49] The bond dissociation energy (BDE) of O_2 is 498 kJ mol^{-1}, larger than the BDE of many typical nonmetal−O bonds such as H−O (430 kJ mol^{-1}), Cl−O (267 kJ mol^{-1}), and F−O (220 kJ/mol).[50,51] The dissociation of O_2, therefore, would be more energetically favorable to process on a catalyst surface with moderate adsorption energy of O_2 through various intermediates such as adsorbed O (O_{ad}), superoxide ion (O_2^-) and $HO_{2,ad}$, among others. The more energetically favorable path is the superoxo/peroxo path, noting that the BDE of O_2^- and O_2^{2-} is around 399 kJ/mol.[52] H_2O_2 easily transforms into HO_2^- in alkaline media according to its pK_a value of 11.7.[53] A reaction scheme taking into account O_2^- and $HO_{2,ad}$ is given in Figure 7, where the first electron transfer

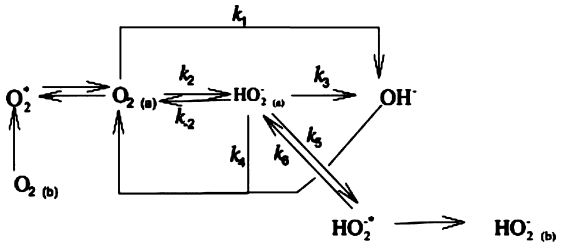

Figure 7. Serial pathway of oxygen reduction on gold surfaces with (a) and without (b) adsorbed species. The subscripts a and b denote the adsorbed and the bulk species, respectively. The superscript (*) refers to the electrode-vicinity species. Reprinted with permission from ref 83. Copyright 2013 Elsevier.

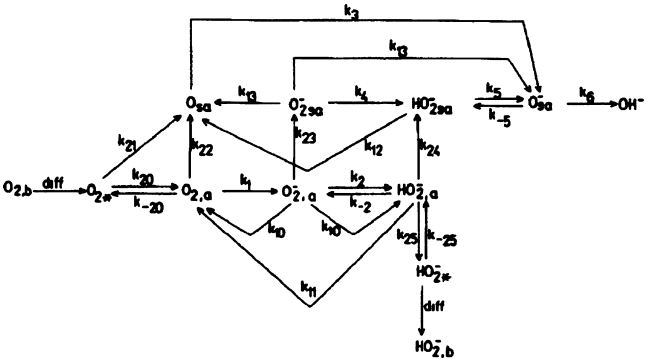

Figure 8. General reaction scheme of oxygen reduction on Pt-based catalyst surface. The subscripts sa, a, b, and * denote "strongly adsorbed", "weakly adsorbed", "bulk", and "the vicinity of disk electrode", respectively. Reprinted with permission from ref 33. Copyright 1987 Elsevier.

(k_1) is usually considered to be the RDS.[54] Figure 8 illustrates a more sophisticated oxygen reduction scheme on Pt-based catalysts, in which no single reaction step involves the exchange of more than one electron. The elementary reaction pathways are[33]

$$O_{2,a} + e^- \xrightarrow{k_1} O_{2,a}^- \quad (17)$$

$$O_{2,a}^- + H_2O + e^- \underset{k_2,k_{-2}}{\longleftrightarrow} HO_{2,a}^- + OH^- \quad (18a)$$

$$2O_{2,a}^- + H_2O \xrightarrow{k_{10}} O_{2,a} + HO_{2,a}^- + OH^- \quad (18b)$$

$$O_{2,a} \xrightarrow{k_{22}} 2O_{sa} \quad (19)$$

DOI: 10.1021/acscatal.5b00524
ACS Catal. 2015, 5, 4643−4667

$$O_{sa} + e^- \xrightarrow{k_3} O_{sa}^- \quad (20)$$

$$O_{2,a}^- \xrightarrow{k_{23}} O_{2,sa}^- \quad (21a)$$

$$O_{2,sa}^- + H_2O + e^- \xrightarrow{k_4} HO_{2,sa}^- + OH^- \quad (21b)$$

$$O_{2,sa}^- \xrightarrow{k_{13}} O_{sa} + O_{sa}^- \quad (21c)$$

$$HO_{2,sa}^- + e^- \underset{k_5,k_{-5}}{\longleftrightarrow} O_{sa}^- + OH^- \quad (22a)$$

$$2HO_{2,sa}^- \xrightarrow{k_{11}} O_{2,a} + 2OH^- \quad (22b)$$

$$HO_{2,sa}^- \xrightarrow{k_{12}} O_{sa} + OH^- \quad (22c)$$

$$O_{sa}^- + H_2O + e^- \xrightarrow{k_6} 2OH^- \quad (23)$$

The first electron transfer steps to adsorbed oxygen species (e.g., $O_{2,a}$, $O_{2,sa}$, O_{sa}, etc.) with or without rapid proton transfer (reactions 17, 19, and 20) are widely regarded as the RDS on Pt surfaces.[55,56] The first electron transfer step to $O_{2,ad}$ is surface-sensitive. It proceeds through reaction 17 on a mercury electrode in the presence of strong surfactants such as triphenylphosphine oxide (TPPO), where those surfactants displace H_2O from the electrode surface and inhibit the normal formation of HO_2^- species. The lifetime $O_{2,a}^-$ is sufficiently long before its decomposition to O_2 and HO_2^- (half-life $\tau_{1/2} \approx 1$ min at pH 13), so that $O_{2,a}^-$ could be seen in the reverse sweep of cyclic voltamograms.[57] The formation of $O_{2,a}^-$ was observed at $E^0 = -0.3 \pm 0.03$ V vs SHE with both O_2 and $O_{2,a}^-$ remaining in the aqueous phase,[58] and the potential did not change from pH 1 to pH 13 on Ag(111) surface in aqueous solutions.[52] The pH-independence caused the overpotential of $O_2/O_{2,a}^-$ to decrease from 1.53 V at pH 0 to 0.7 V at pH 14, noting that the standard reduction potential of H_2O/OH^- changed from 1.229 to 0.401 V as the pH value changes from 0 to 14.[5,52] The decrease of η is one of the reasons to explain the wide availability of catalysts for the alkaline media. The first protonation step of O_2 (reactions 18a, 18b, and 21a) does not involve the cleavage of O−O bond of precious-metal-based catalysts.[4,35,54] The followed reactions proceed either via a two-electron ($2e^-$) pathway or a four-electron ($4e^-$) pathway. Although a two-electron ($2e^-$) pathway followed by disappropriation of HO_2^- (reactions 2 + 3a) can be detected by RRDE, it is hard to discriminate the nuance between a two-electron pathway followed by fast in situ electrochemical elimination of HO_2^- ("serial" $2e^- + 2e^-$ pathway, reactions 2 + 3b) and a $4e^-$ pathway ("direct" pathway, reaction 1). For example, part of O_2 was partially reduced to HO_2^-, but the HO_2^- was almost simultaneously further reduced to OH^- on Pt/C catalysts that were supported on porous gas diffusion layer.[59] In the literature, a so-called "pseudo" $4e^-$ pathway is always claimed by researchers without differentiating the $2e^- + 2e^-$ pathway with the $4e^-$ pathway.[60] A direct approach on supporting a proposed reaction scheme is to in situ detect the reaction intermediates. Surface-enhanced infrared reflection absorption spectroscopy detected a potential-dependent vibration band at 1005−1016 cm^{-1} of Pt surfaces in 0.1 M $NaClO_4$ + NaOH (pH 11) solution, which was assigned to the O−O stretching mode of O_2^-.[61] The O−O stretch mode of O_2^- was also observed on polycrystalline Au surface in 0.1 M NaOH solution by surface-enhanced Raman spectroscopy at the frequency of 1150 cm^{-1}.[50] The detection of O_2^- but no detection of HO_2^- implied that the protonation of O_2^- (reaction 21a) was the RDS of the $2e^- + 2e^-$ pathway for precious metal catalysts.

2.3. Reaction Pathways on Transition Metal Oxides. The ORR reaction pathways at transition metal oxide surfaces follow a different rationale to those at precious metal surfaces. The surface cations of transition metal oxides coordinate with the oxygen of H_2O in order to fulfill their full oxygen coordination. The hydrogen atoms of H_2O become distributed over the catalyst surface. To create OH^- species, the protonation of surface oxygen ligand is charge-compensated by the reduction of a surface cation M such as Mn^{4+}, Co^{3+}, Fe^{3+}, and so forth. The M−OH^- species further interact with O_2 which adsorb on oxide surfaces with either end-on or side-on configurations.[1] The ORR pathways on oxide surfaces would be[62]

$$2M^{m+} - O^{2-} + 2H_2O + 2e^- \rightarrow 2M^{(m-1)+} - OH^- + 2OH^- \quad (24)$$

$$O_2 + e^- \rightarrow O_{2,ads}^- \quad (25)$$

$$2M^{(m-1)+} - OH^- + O_{2,ads}^- + e^- \rightarrow 2M^{m+} - O^{2-} + 2OH^- \quad (26)$$

or more probably

$$M^{m+} - O^{2-} + H_2O + e^- \rightarrow M^{(m-1)+} - OH^- + OH^- \quad (27)$$

$$O_2 + e^- \rightarrow O_{2,ads}^- \quad (28)$$

$$M^{(m-1)+} - OH^- + O_{2,ads}^- \rightarrow M^{m+} - O - O^{2-} + OH^- \quad (29)$$

$$M^{m+} - O - O^{2-} + H_2O + e^- \rightarrow M^{(m-1)+} - O - OH^- + OH^- \quad (30a)$$

$$M^{(m-1)+} - O - OH^- + e^- \rightarrow M^{m+} - O^{2-} + OH^- \quad (30b)$$

$$M^{m+} - O - O^{2-} + H_2O + e^- \rightarrow M^{(m-1)+} - OH^- + HO_2^- \quad (30c)$$

where reactions 26 and 30c are RDS.[62] A schematic presentation of reaction pathways are illustrated in Figure 9. The interaction of O_2 with metallic oxide catalysts can be explained by the inorganic chemistry principles of molecular orbitals and crystal field theory. By studying the ORR activities of transition metal (TM)-doped lanthanum nickel oxides and oxides with metallic conductivity, Matsumoto et al. found that

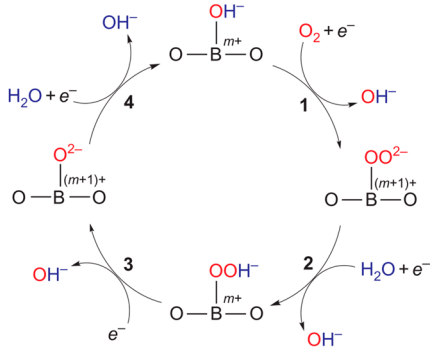

Figure 9. Proposed ORR mechanism on perovskite oxide catalysts. The ORR process via four steps: 1, surface hydroxide displacement; 2, surface peroxide formation; 3, surface oxide formation; 4, surface hydroxide regeneration. Reprinted with permission from ref 65. Copyright 2011 Nature Publishing Group.

DOI: 10.1021/acscatal.5b00524
ACS Catal. 2015, 5, 4643−4667

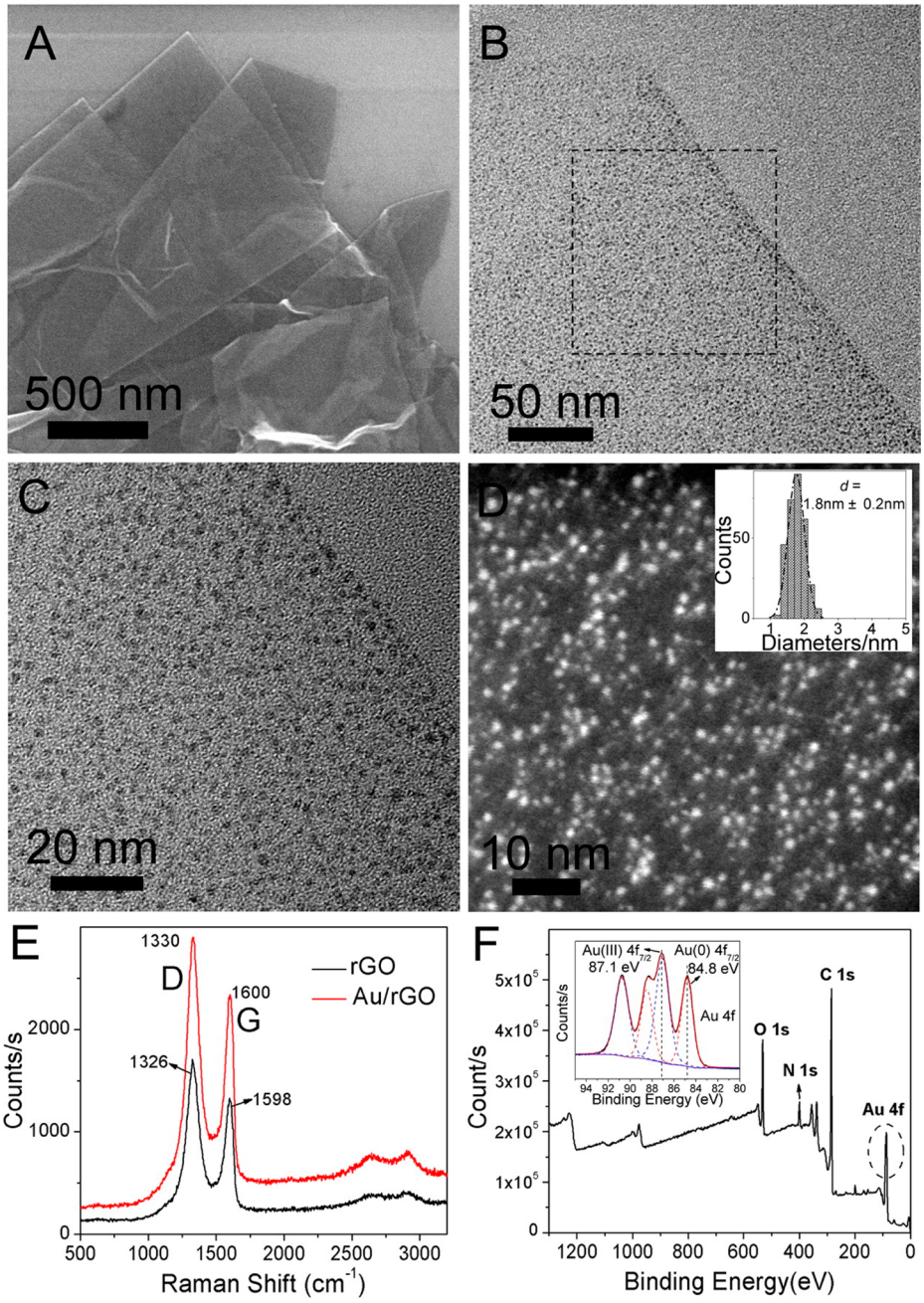

Figure 10. (A) SEM image, (B,C) TEM, (D) HAADF, (E) Raman spectrum, and (F) XPS spectrum of as-synthesized Au/rGO hybrids. Inset in panel D stands for the statistic histogram of Au cluster sizes, whereas the inset in panel F represents the XPS spectrum of the Au element in Au/rGO hybrids.[87]

the catalytic activity was influenced by the overlap integral between the e_g orbital of TM and the sp_σ orbital of oxygen and that the larger the overlap integral, the higher was the electrocatalytic activity.[63,64] Yeager proposed that a strong metal-to-oxygen interaction was established by the overlapping of the π orbitals of O_2 with the d_{z^2} orbitals of a TM element, with back-bonding from at least partially filled d_{xz} or d_{yz} orbitals of TM to the π^* orbitals of O_2. The strong TM−O interaction resulted in a weakening of the O−O bond and led to the dissociative adsorption of O_2 and probably simultaneous protonation and valence change of TM.[35] In 2011, the Shao-Horn group observed a volcano plot of the catalytic activities of perovskite oxides versus the e_g electrons that peaked at e_g electrons ca. 0.8−1.0. A moderate e_g filling around 0.8−1.0 conferred the B−O_2 bonding that was neither too strong nor too weak. The presence of an e_g electron was proposed to destabilize the TM−O bond and together with $O_{2,ad}^-$ to facilitate the displacement of OH^- of TM−OH^- with TM−O_2^{2-} (reaction 28).[65] During oxygen incorporation, Mueller et al. noticed that the surface lattice oxygen anion of perovskite oxides was oxidized while the oxygen adsorbate was reduced, highlighting the crucial role of anion-redox chemistry of the surface of transition metal oxides during ORR.[66]

3. CATALYSTS FOR OXYGEN REDUCTION REACTION

3.1. Precious Metals. *3.1.1. Platinum.* No single polycrystalline metal catalyzes the ORR as effectively as Pt.[67] Extensive works on Pt single crystals and Pt nanoparticles

DOI: 10.1021/acscatal.5b00524
ACS Catal. 2015, 5, 4643−4667

supported on a carbon black matrix (Pt/C) were carried out in acidic media,[25,68,69] given its excellent activity and the extensive interests on its technical application in acidic polymer electrolyte fuel cells. Research works on Pt/C in alkaline media attract more and more attention because of the increasing interests on alkaline fuel cells and batteries. The Pt particle size of Pt/C has substantial influence on its activity for ORR in alkaline media. A plot of mass activity (MA) of thin film Pt showed MA reached maximum at 2 nm-thick Pt film with an average particle size of 3 nm.[70] A 3-fold reduction in activity was observed when Pt particles decreased in size from 24 to 2 nm in 1 M NaOH solution.[41] This decrease in activity was attributed to excess HO_2^- on the surface, which was desorbed into bulk solution and without further reduction. In contrast, a combined experimental and thin film/flooded agglomerate model analysis by Gonzalez et al. indicated the highest MA of Pt/C with Pt particle size of 5 nm and the highest specific activity of Pt/C with Pt particle size of 4 nm in 1 M NaOH solution.[71] A desirable Pt particle around 4−5 nm was also observed in a 20 wt % Pt supported on microporous-mesoporous carbon derived from molybdenum carbide (Pt(20 wt %)/C(Mo_2C)), whose ORR kinetics in 0.1 M KOH solution was better than commercial Pt (20 wt %)/Vulcan on electrochemical surface area (ECSA) basis.[72,73] The further increase of Pt loading to 60 wt % showed little improvement of Pt(60 wt %)/C(Mo_2C) as compared to Pt(60 wt %)/Vulcan.[74]

To reduce the use of high-cost Pt, core−shell structures with Pt as shell and less costly metal as core were developed, such as Pt@Au nanorods dispersed on pyridine cycloaddition of graphene (Pt@Au-PyNG) and Pt@Pd nanocubes enclosed with (100) planes.[75,76] Another approach is to use nonprecious metal oxides as the catalyst support for Pt. A novel Pt cluster loaded on $CaMnO_3$ as a noncarbon support was developed. It exhibited essentially competitive ORR kinetics of commercial Pt/Vulcan and outperforms Pt/C with better operating durability.[77] Tin-doped indium oxide (ITO) is a well-known conducting glass material. Pt with particle size of 5 nm was coated on 22 nm ITO nanoparticles by galvanic replacement of electrodeposited Cu layer. The interaction between Sn atoms with Pt at the Pt/ITO interfaces was reported in the literature and confirmed by the −0.3 V negative shift of the Sn and In X-ray photoelectron spectroscopy (XPS) peaks of Pt/ITO catalysts. This atomic-level interaction between Pt and ITO would be the reason for the salient MA, specific activity, and operating durability of Pt/ITO, all of which are better than Pt/Vulcan.[78]

The catalytic activity and efficiency of ORR on the Pt surface in alkaline media is lower than in the acidic one, mainly due to the excessive HO_2^- species generated on the Pt surface in alkaline solutions.[41] Moreover, the future of Pt/C is shadowed with high cost, scarcity, and the insufficient durability of Pt. Recent works have recognized some non-Pt metals and alloys for ORR.

3.1.2. Gold. Au (100) is the most active crystalline facet of Au single crystals for the ORR in alkaline media, albeit a poor catalyst in acidic media. The η for oxygen reduction on Au (100) in 0.1 M NaOH is 0.34 V.[79] Such a small η value is even better than η = 0.48 V of Pt (110) in 0.1 M $HClO_4$.[80] DFT calculations indicated the rate of the reactions after the transfer of first electron (reactions 15 or 18) were fast enough to render the very small concentration of O_2^-.[81] O_2^- were attracted to the surface of Au(100) that was positively charged at small η, where they reacted rapidly.[82] Polycrystalline Au and Au electrodeposited on Ni substrate both showed desirable catalytic activity for HO_2^- reduction.[39] This indicates that ORR could proceed on the Au surface via $2e^- + 2\ e^-$ pathway or 4 e^- pathway. Awad and Ohsaka developed a method to electrodeposit Cu nanoparticles on the Au(111) facet, and the ORR active Au(100) and Au(110) were protected by a cysteine monolayer. The cysteine monolayer was later completely removed by the reductive desorption in 0.5 M KOH. In that way, the nano-Cu/Au was a $4e^-$ ORR catalyst with a slightly less negative ORR reduction peak compared to Pt.[83]

Au is relatively inert in the bulk polycrystalline state but exhibits good catalytic activity at the nanoscale.[84] Nanosized Au needs suitable catalyst supports such as carbon blacks. Graphene was reported as a more stable and robust catalyst support than the conventional Vulcan carbon.[85] Specific activity of an Au/reduced graphene oxide (rGO) nanocomposite was three times higher than that of Au nanoparticles.[86] Figure 10 shows an Au cluster/reduced graphene oxide hybrid (Au/rGO) with mean Au size of 1.8 nm obtained by a surfactant-free synthesis method. Although the ORR kinetics of Au/rGO was inferior to the commercial Pt/C, Au/rGO outperformed Pt/C with better operating stability and methanol tolerance. Pt/rGO and Pd/rGO could be synthesized by the same method.[87] An Au/rGO with uniformly distributed Au clusters with particle sizes less than 2 nm was synthesized by using citric acid as the reducing and linking agent. A composite catalyst consisting of freestanding and stretchable thin-film of Au nanoparticles (∼10) nm decorated on reduced graphene oxide (rGO) was synthesized by a polystyrene-poly(4-vinylpyridine) diblock copolymer micelle method.[88] The ORR kinetics of Au(10 nm)/rGO was relatively poor, as reflected from the E_{onset} of −0.2 V vs Ag/AgCl, possibly due to the use of poorly conducting polymer surfactant.

Alloying Au with less costly metal noble metals, such as Ag, is a viable approach to reduce the cost of ORR catalysts. A volcano plot of the composition effect of AgAu alloy catalysts with particle sizes of 3−5 nm was reported, showing that the catalyst with 36 at. % Au gave the best activity.[46] Chen et al. reported a Langmuir−Blodgett method as well as galvanic exchange reaction to prepare AgAu Janus particles. Despite a minimal loading of Au on Ag, specific activity and MA of ORR of the resulting Janus particles were 6−7 times that of the Ag nanoparticles.[89]

3.1.3. Palladium. Pd is active for ORR in alkaline media. A combined electrochemical and topological analysis indicated that polycrystalline Pd surfaces underwent pronounced surface oxidation/reduction and morphology evolution due to the interaction of Pd with surface species, as listed in reactions 17−23.[90] A RDE study on the relationship between ORR activity and d-band center of noble metals (i.e., Au, Ag, Pd, Rh, Ir, Ru and Pt) indicated close d-band center value between Pd(111) and Pd/C with Pt(111) and Pt/C.[91] The specific activity of (100)-oriented Pd nanocubes with particle size of 27 nm was ∼4 times of that of spherical Pd nanoparticles with particle size of 3 nm, highlighting the high activity of Pd(100) in alkaline media.[92] Recently, 14 nm Pd nanocubes with (100) facets and with (111) facets at corners were synthesized. The adsorption of OH^- on the truncated Pd nanocubes in 1 M NaOH was more significant than in 0.1 M NaOH.[93]

A number of different methods have been utilized for synthesizing Pd nanoparticles on carbon supports, including the reduction,[92,94,95] electrodeposition,[96] evaporation.[97] Similar to Pt/C, the particle size of Pd of Pd/C is nontrivial. The specific

DOI: 10.1021/acscatal.5b00524
ACS Catal. 2015, 5, 4643−4667

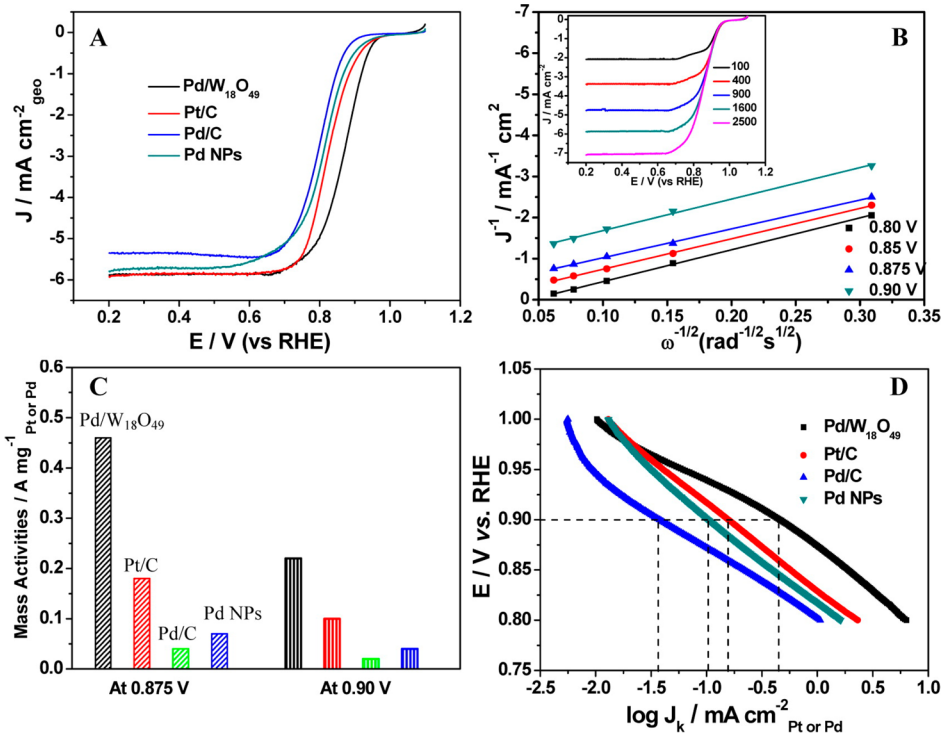

Figure 11. (A) ORR polarization curves on the strongly coupled $Pd/W_{18}O_{49}$ hybrids, Pt/C, Pd/C, and the supportless Pd nanoparticles in O_2-saturated 0.1 M KOH solution at room temperature, with rotation rate of 1600 rpm and a potential sweep rate of 10 mV/s. (B) Koutecky–Levich plots on $Pd/W_{18}O_{49}$ at different potentials. Symbols are experimental data from the corresponding rotating-disk voltammograms shown in the inset. Lines are the linear regressions. (C) Mass activities for $Pd/W_{18}O_{49}$, Pt/C, Pd/C, and the supportless Pd nanoparticles at 0.875 and 0.90 V. (D) Tafel plots from the different electrocatalysts and the comparison of their specific activities.[102]

activity of Pd/Vulcan for ORR increased continuously by 3 times with increased Pd particle sizes from 3.1 to 16.7 nm. In contrast, MA of Pd/Vulcan reached a maximum of Pd(5 nm)/Vulcan, which was about 30% better than the untreated Pd/Vulcan.[98] This was scribed to the stronger adsorption of hydroxyl species on very small particles (<5 nm) that block the active reaction sites,[98] similar for the case of Pt.[41,70,71] Tammeveski et al. prepared Pd/multiwalled carbon nanotubes (MWCNTs) by the magnetron sputtering of Pd nanoparticles on MWCNTs.[99] An optimized annealing temperature of 500 °C was identified for Pd/MWCNTs, albeit larger particle sizes of Pd after the annealing at 500 °C than 300 and 400 °C. The phenomenon that the specific activity (SA = j_K/ESCA) decreases with decreasing particle size of Pd has been attributed to the stronger adsorption of hydroxyl species on smaller particles, which blocks the active sites for ORR.[99] A number of works on dispersing Pd nanoparticles on various catalyst supports have been reported. Pd/nitrogen-doped graphene oxide (NrGO) was synthesized by using $NaBH_4$ as the reducing agent.[100] The formation of HO_2^- during ORR was negligible for Pd/Vulcan and Pd/NrGO,[98,100] implying a dominant $4e^-$ pathway. The enhanced ORR activity of Pd-rGO was attributed to the tensile strain effect when Pd contacted graphene, which resulted in the electron exchange transfer between Pd and graphene interfaces and increased the interaction states and transmission channels between Pd and graphene while keeping sufficient π electrons on graphene for conduction.[101] Chen et al. developed a hybrid catalyst consisting of Pd nanotetrahedron and $W_{18}O_{49}$ nanosheets ($Pd/W_{18}O_{49}$). $E_{1/2}$ of $Pd/W_{18}O_{49}$ was 40 mV more positive than that of Pt/C (Figure 11). The impressive ORR performance of $Pd/W_{18}O_{49}$ was attributed to the strong coupling between Pd and $W_{18}O_{49}$, where the strong oxygen affinity of Pd was weakened by $W_{18}O_{49}$ and moderate dissociative adsorption energy of O_2 on Pd surface was attainted.[102] Sato et al. reported amorphous PdP nanoparticles supported on glassy carbon electrodes were highly active for ORR.[96]

Alloying Pd with transition metals improves the catalytic activity as well as reducing the use of Pd. Han et al. reported the synthesis of MPd_3/rGO (M = Fe, Cu, Ag, Au, Cr, Mo, W) by the hydrogen annealing of Pd and M-anchored poly(diallyldinethylammonium chloride) (PDDA)-functionalized GO. MPd_3 nanoparticles were uniformly distributed, and their particle sizes were between 3–9 nm. The ORR onset potentials of MPd_3/rGO are found to follow the order: $CuPd_3$ < $AgPd_3$ < $CrPd_3$ < $MoPd_3$ < WPd_3 < $AuPd_3$ < $FePd_3$.[103] Recently, 5-fold twinned Pd_2NiAg with a Ni-terminated surface was developed for ORR application. The improved ORR activity was attributed to the decreased oxygen adsorption energy of the 15 nm Pd_2NiAg nanocrystals over PdAg alloys.[104]

Apart from the alloying method, constructing core–shell structure with Pd as shell material is another viable method. A silver core/Pd shell (Ag@Pd) structure supported on MWCNT was synthesized by galvanic displacement of Pd on Ag, but it performed worse than commercial Pd/C for the ORR in 1 M KOH.[105] In contrast, an Au core/Pd shell structure supported on rGO (Au@Pd/rGO) exhibited almost doubled MA as compared to Pd black.[106] The conflicting results underline the influence of synthesis routes and catalyst/support interactions, which result in different surface quality and structures, on determining the catalytic activity.

DOI: 10.1021/acscatal.5b00524
ACS Catal. 2015, 5, 4643–4667

Table 1. ORR Performance of Precious-Metal-Based Catalysts Obtained from RDE[a]

catalysts	E_{onset} vs RHE[b]	$E_{1/2}$ vs RHE	Tafel slope (mV/decade)	durability	ref
Pt (20 wt %)/C	1.07		−57 (low j);		71
	0.91		−120 (high j)		
Pt/Vulcan	0.93****		−60 (low j);		72
	0.79****		−81 (high j)		
	(3000 rpm)				
Pt/C(Mo_2C)	1.06****		−60 (low j);		
	0.83****		−88 (high j)		
	(3000 rpm)				
Pt/$CaMnO_3$	0.95		−65 (low j);	95% retention of j under 0.80 V for 27.8 h	77
	0.81		−109 (high j)		
Pt@Au/PyNG	0.92			99% retention of j after 1000 CV scans	75
	undefined				
Pt@Pd	0.97			80% retention of j after 1000 cycles from 0.13 to 1.14 V	76
	0.88				
	(1 M NaOH)				
Pt/ITO	0.96		−69 (low j);	20 mV penalty of $E_{1/2}$ after 300 cycles from 1.11 V to 0.51 V	78
	0.82		−129 (high j)		
Au(100)	0.96****				79
	0.80****				
Au(110)	0.84****				
	0.70****				
Au(111)	0.84****				
	0.67****				
Au (1.8 nm)/rGO	0.88*			84% retention of j under 0.78 V for 11.1 h	87
	undefined				
Au (<2 nm)/rGO	0.83**			84% retention of j after 1000 CV scans from −0.04 to 1.16 V	84
	undefined				
Au/rGO	0.85**			95% retention of j under 0.80 V for 13.9 h	86
	0.70**				
Janus AgAu	0.92		−117 (low j);		89
	0.77		−263 (high j)		
Au(36 at.%)/Ag	0.92		−62 (low j);		46
	0.76		−109 (high j)		
Pd	1.00		−65 (low j);		90
	0.89		−124 (high j)		
Pd (2.6 nm)	0.98		−67 (low j);		100
	0.82		−129 (high j)		
Pd nanocube	1.00		−79 (low j);		92
	0.87		−180 (high j)		
	(1900 rpm)				
Pd/C	0.97****		−60 (low j);		98
	0.86****		−125 (high j)		
Pd/rGO	0.93			negligible penalty of $E_{1/2}$ after 4000 cycles from 0.86 V to 0.36 V	101
	0.73				
PdP	0.97			58% retention of j under 0.80 V for 8.3 h	96
	0.85				
$FePd_3$/rGO	0.93***				103
	0.75***				
Pd/$W_{18}O_{49}$	0.98				102
	0.86				
Pd/MWCNT	0.96		−74 (low j);		99
	0.81		−130 (high j)		
	(1900 rpm)				
Pd_2NiAg	0.97*			negligible penalty of $E_{1/2}$ after 5000 cycles from 0.18 V to 1.08 V	104
	0.83*				
Ag@Pd/MWCNTs	0.83****			50% retention of specific current under 0.82 V for 0.5 h	105
	0.72****				
	(1 M KOH)				
Au@Pd/rGO	0.90***			10 mV penalty of $E_{1/2}$ after 1000 cycles from 1.01 to 0.22 V	106
	0.70***				
Ag(110)	0.91		−80 (low j);		111

DOI: 10.1021/acscatal.5b00524
ACS Catal. 2015, 5, 4643−4667

Table 1. continued

catalysts	E_{onset} vs RHE[b]	$E_{1/2}$ vs RHE	Tafel slope (mV/decade)	durability	ref
	0.70		−123 (high j)		
Ag(111)	0.88		−85 (low j);		52
	0.64		−125 (high j)		
Ag(20 wt %)/C	1.02				115
	0.87				
Ag (4.5 nm)	0.84**				112
	0.63**				
Ag@Pt@Ag	0.89*		−80 (low j);		43
	0.69*		−120 (high j)		
Ag/CNT	0.85**				116
	0.74**				
Ag/GO/C	0.83				119
	0.70				
Ag/GO-S-$(CH_2)_2$−SH	0.88*		120		117
	0.67*				

[a]The rotating rate of RDE is 1600 rpm, and the electrolyte is O_2-saturated 0.1 M KOH/NaOH, unless otherwise stated. [b]: η_{onset} is readily calculated from E_{onset} by $\eta_{onset} = 1.227\ V - E_{onset}$. *: converted from Ag/AgCl in 3 M KCl, $E_{vs\ RHE} = E_{vs\ Ag/AgCl} + 0.209\ V + 0.059 \times pH$. **: converted from Ag/AgCl in saturated KCl, $E_{vs\ RHE} = E_{vs\ Ag/AgCl} + 0.197\ V + 0.059 \times pH$. ***: converted from saturated camel electrode, $E_{vs\ RHE} = E_{vs\ SCE} + 0.241\ V + 0.059 \times pH$. ****: converted from Hg/HgO electrode, $E_{vs\ RHE} = E_{vs\ MMO} + 0.098\ V + 0.059 \times pH$.

3.1.4. Silver. Due to the high-cost of Pt, Au, and Pd, there are growing interests in exploring relative more cost-effective metallic catalysts. Ag is a promising candidate because it has similar reaction mechanisms and kinetics for ORR compared to Pt.[107,108] Ag is also a good HO_2^- elimination catalyst.[109,110] ORR on Ag single crystal surfaces and Ag nanoparticles proceeded through the pseudo $4e^-$ pathway.[111,112] ORR proceeded by the $4e^-$ pathway on Ag/Vulcan with large Ag nanoparticles (174 nm) but the $2e^- + 2e^-$ pathway on that with small Ag nanoparticles (4.1 nm).[113] The higher fractional contribution of the $2e^-$ pathway of polycrystalline Ag was attributed to a more defective surface of bulk Ag, at which stronger adsorption of OH^- prevented the two-site chemisorption of O_2 that was needed for the $4e^-$ pathway. The ORR kinetics of different facets of Ag single crystal increases in the order Ag(100) ≤ Ag(111) ≤ Ag(110).[112] Two opposing effects, the adsorption of spectator OH^- and the activation energy, were well balanced for Ag(110), which was the most active Ag facet.[111] Weaker adsorption of hydroxide species on Ag(111) than that on Ag(100) was confirmed by the investigation on Ag(111)-terminated nanodecahedra and Ag(100)-terminated nanocube.[114]

The best composition and Ag loading of Ag supported on carbon materials are still under debate. Coutanceau et al. stated 20 wt % of Ag as the best composition of Ag/C in terms of current density and MA.[115] Fazil and Chetty found 40 wt % Ag was the best loading of Ag/CNT nanocomposites.[116] In contrast, Chen et al. found the ORR activity of Ag/C was relatively insensitive to the Ag loading from the range of 10 wt % to 60 wt %, although a mild positive shift of E_{onset} was observed among catalysts with increasing Ag loading.[108] Besides carbon blacks, graphene has been recently used for two-dimensional (2D) and three-dimensional frameworks (3D) with Ag catalysts, such as Ag/GO linked by thiols,[117] Ag/rGO linked by deoxyribonucleic acid (DNA),[118] and 3D GO/carbon supported Ag composite (Ag/GO/C).[119] E_{onset} and $E_{1/2}$ of these Ag/nanocarbon catalysts are generally about 50−100 mV more negative than Pt(20 wt %)/Vulcan.[116−119] Ag nanoparticles were also used for improving the electrical conductivity and catalytic activity of transition metal oxides such as MnO_x.[120,121] Table 1 lists the ORR performance of Pt, Au, Pd, and Ag-based catalysts.

3.2. Carbon. *3.2.1. Nonmetal Doped Carbon.* Carbon, including carbon black, graphene, and carbon nanotube (CNT), is conventionally used as catalyst support because of its high electronic conductivity and large surface area. The chemically stable sp^2 hybridized carbon atoms in graphene and CNT hinder their more broad application as electrocatalyst. Recently, it is noticed that carbon doped with nonmetal heteroatoms exhibits good ORR activity, where the nonmetal elements include N, B, S, P, F, and so forth. Besides N, other popular dopants include B, P, S, and F. Although the exact mechanisms were still under debate, the inclusion of heteroatoms was believed to create carbon active sites adjacent to the heteroatoms and facilitated the O═O bond breaking of O_2 after the modulation of the binding energy of oxygen.[122−124] Paraknowitsch and Thomas gave an excellent review on the B-doped, P-doped, and S-doped carbons for fuel cell applications.[125] Very recently, Dai et al. gave an exhaustive review on nanocarbons (e.g., fullerenes, CNT, graphene), the use of nanocarbons for oxygen electrocatalysis, intermolecular charge transfer, spin redistribution of nanocarbon catalysts and their applications in fuel cells.[126] To avoid duplicating the above work, section 3.2.1 reviews the very recent progress on doped and codoped carbons with heteroatoms for ORR in alkaline media.

Nitrogen-doped carbon (NC), including N-doped carbon nanofiber (N-CNF),[127] N-doped carbon nanotube (N-CNT), N-doped graphene (NGR), and N-doped carbon black, is one of the most studied heteroatom-doped carbons for ORR.[122] The introduction of N atoms into carbon increases the electronic density of states near the Fermi level, thus facilitating the electronic transfer from the electronic bands of C to O_2 σ^* antibonding orbitals.[128,129] For the case of N-CNF and N-CNT, Maldonado and Stevenson found ORR proceeds via the $2e^-$ pathway followed by catalyzed disproportionation of HO_2^- (reaction 3b) and highlighted the exposed edge plane defects and N-doping sites as "hot spots" for ORR.[60,130] For the case of NGR, the spin density and charge distribution of carbon atoms are influenced by the neighboring nitrogen, which induces activated regions on the graphene surface.[131] The ORR activity

DOI: 10.1021/acscatal.5b00524
ACS Catal. 2015, 5, 4643−4667

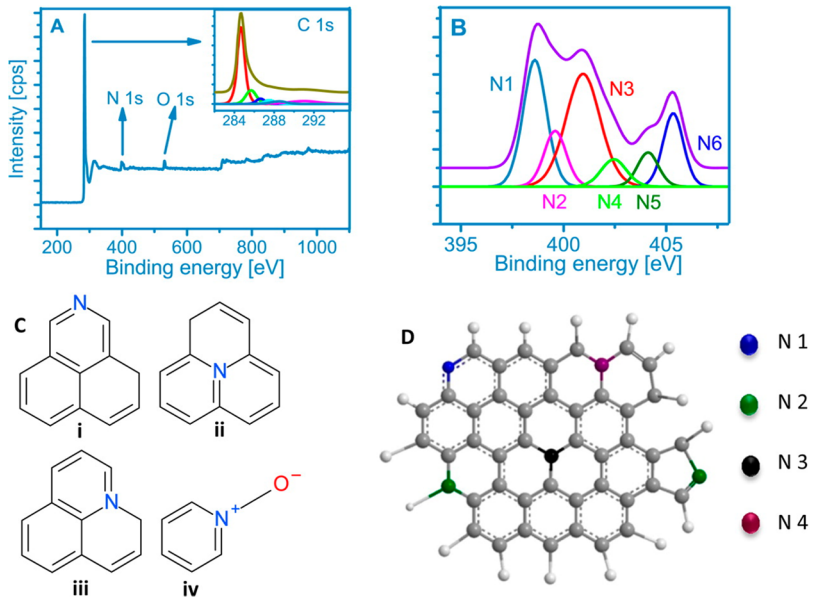

Figure 12. (A) Typical XPS spectrum of nitrogen-doped CNT with assigned peaks. Inset: high-resolution C 1s peak, (B) high-resolution N 1s peak, (C) possible nitrogen positions in the structure; (i) top-N, (ii) center-N, (iii) valley-N, and (iv) oxide-N. (d) different nitrogen functionalities in a graphitic sheet: pyridinic-N (N1), pyrrolic-N (N2), graphitic-N in center (N3, N-Q_{center}), and graphitic-N in valley (N4, N-Q_{valley}).[135]

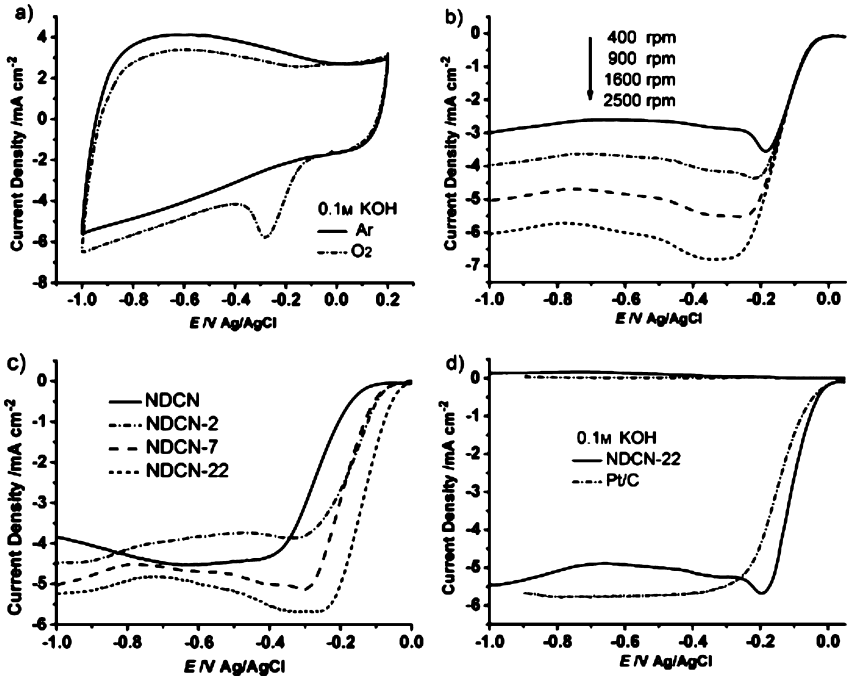

Figure 13. (a) CV of nitrogen-doped carbon nanosheets derived from silica-22 (NDCN-22) in Ar- and O_2-saturated 0.1 M KOH solution at a scan rate of 100 mV s^{-1}. (b) Linear sweep voltammetry (LSV) of NDCN-22 in O_2-saturated 0.1 M KOH at a scan rate of 10 mV s^{-1} at different RDE rotation rates. (c) LSV of the NDCN and NDCN-X in O_2-saturated 0.1 M KOH at a scan rate of 10 mV s^{-1} with an RDE rotation rate of 1600 rpm. (d) RRDE polarization curve for NDCN-22 and Pt/C in O_2-saturated 0.1 M KOH at a scan rate of 10 mV s^{-1} with an RDE roration rate of 1600 rpm. For all the rotating disk electrode (RDE) and the rotating ring-disk electrode (RRDE) measurements, the loading of catalysts was 20 μg_{Pt} cm^{-2} for Pt/C and 0.6 mg cm^{-2} for NDCN-X and the NDCN. Reprinted with permission from ref 150. Copyright 2014 Wiley.

of NC originates from the conjugation between the graphene π orbitals and the nitrogen lone-pair.[132] N-sites of NC include pyridinic N, pyrrolic N, and quaternary N. Pyridinic N refers to N atoms at the edges of graphene planes, where each N is bonded to two carbon atoms and donates one p-electron to the aromatic π system. Pyrrolic N atoms are integrated into five-membered heterocyclic rings, which are bonded to two carbon atoms and contribute two p-electrons to the π system. Quaternary N atoms are those substituting carbon atoms within the graphene layer.[133] The pyridinic and pyrrolic N are located at the graphitic edge, where quaternary N can be both "edge-N" and "bulk-like-N".[134] Quaternary N is further classified into quaternary N valley sites (N-Q_{valley}) and quaternary N center cites (N-Q_{center}) (Figure 12).[135] The binding energy (BE) of N 1s increases in the sequence of pyridinic *N* < pyrrolic *N* < quaternary N.[136] Quaternary and

DOI: 10.1021/acscatal.5b00524
ACS Catal. 2015, 5, 4643−4667

Table 2. ORR Performance of Non-Metal-Doped Nanocarbon Catalysts Obtained from RDE[a]

catalysts	E_{onset} vs RHE[b] $E_{1/2}$ vs RHE	durability	ref
nitrogen-doped			
N-doped porous carbon	0.86 0.70	75% retention of j under 0.60 V for 7 h	151
N-doped porous carbon	0.91** 0.79**	71% retention of j under 0.56 V for 2.8 h	145
N-doped mesoporous carbon	0.71 undefined		149
N-doped carbon sheets	0.91 0.73		147
N-rich porous carbon	0.76**** 0.65****	negligible degradation of j under 0.71 V for 1.1 h	132
N-doped carbon nanosheets	0.96* 0.85*		150
N-doped carbon nanofiber	0.95 0.80	20 mV penalty of $E_{1/2}$ after 10 000 cycles from 1.0 to 0.6 V	127
N-doped graphene	0.85** 0.71**		133
N-doped graphene	0.89*** 0.78***		143
N-doped graphene	0.87** 0.71**	72% retention of j under 0.61 V for 5.6 h	142
N-doped graphene	0.95** 0.82**	88% retention of j under 0.71 V for 10 h	146
py-decorated CNT	0.83** 0.69**		140
N-doped unzipped CNT	0.86** 0.68**	94% retention of j under 0.66 V for 1.4 h	141
N-doped CNT	0.77***** 0.59*****		135
N-doped CNT−graphene	0.91*** 0.71***	negligible degradation of E_{onset} and j_L after 1000 cycles from 1.01 to −0.21 V	144
boron-doped or boron as a codopant			
B-doped CNT	0.75*** undefined****		152
B- and N-doped nanodiamond	0.93*** 0.81*** (1900 rpm)	95% retention of j under 0.81 V for 13.9 h	155
B- and N-doped graphene quantum dot/graphene	0.91** 0.76**		157
B- and N-doped carbon nanoribbon	1.09** 0.93**		156
B- and N-doped CNT	0.91*** 0.76***	90% retention of j under 0.71 V for 13.9 h	153
sulfur-doped or sulfur as a codopant			
S-doped graphene	0.90** undefined		159
S- and N-doped graphene	0.89* undefined		164
S- and N-doped graphene	0.83* undefined		160
S- and N-doped CNT	0.96*** 0.81***		162
S- and N-doped carbon	1.06** 1.01**		163
others			
P-doped carbon hollow sphere	0.88* 0.76*	93% retention of j under 0.68 V for 16.7 h	165
P- and N-doped biocarbon	0.94 0.82	85% retention of j under 0.75 V for 12 h	166
N-, P-, and B-doped carbon	0.86*** 0.73***	95% retention of j under 0.71 V for 10 h	167
F-doped carbon	0.98***	negligible degradation of E_{onset} and j_L after 12 000 cycles from 1.31 to −0.19 V	168

DOI: 10.1021/acscatal.5b00524
ACS Catal. 2015, 5, 4643−4667

Table 2. continued

catalysts	E_{onset} vs RHE[b] / $E_{1/2}$ vs RHE	durability	ref
	0.89[***]		

[a]The rotating rate of RDE is 1600 rpm, and the electrolyte is O_2-saturated 0.1 M KOH/NaOH, unless otherwise stated. [b]: η_{onset} is readily calculated from E_{onset} by $\eta_{onset} = 1.227\ V - E_{onset}$. [*]: converted from Ag/AgCl in 3 M KCl, $E_{vs\ RHE} = E_{vs\ Ag/AgCl} + 0.209\ V + 0.059 \times pH$. [**]: converted from Ag/AgCl in saturated KCl, $E_{vs\ RHE} = E_{vs\ Ag/AgCl} + 0.197\ V + 0.059 \times pH$. [***]: converted from saturated camel electrode, $E_{vs\ RHE} = E_{vs\ SCE} + 0.241\ V + 0.059 \times pH$. [****]: converted from Hg/HgO electrode, $E_{vs\ RHE} = E_{vs\ MMO} + 0.098\ V + 0.059 \times pH$.

pyridinic N are generally the most stable N sites at high temperatures (>600 °C).[137] Although the real nature of the roles of various N sites in NC still remains unclear, literature results have showed that different N sites contribute differently to the ORR. Ruoff et al. found the pyridinic N improved E_{onset} and the quaternary N determined j_L, whereas the total N content did not play a vital role in ORR.[133] Comparing a series of NGR, the authors also thought graphitic-N dominated NC had higher catalytic activity with larger j_L than pyrrolic-N or pyridinic-N dominated NC.[133] Giambastiani et al. found CNT functionalized with 9-aminoacridine (a mimic of pyridine framework) showed more positive E_{onset} and larger j_L than that functionalized with 3-aminocarbazole (a mimic of pyrrole framework).[138] Wågberg et al. reported the thermal treatment of N-doped MWCNTs transformed pyrrolic and pyridinic N sites into quaternary N sites, and confirmed an overall improvement of ORR performance.[135] N sites located at the graphitic edge planes were reported to be highly efficient for ORR.[134] The 4 e^- pathway occurred on the N edge defects (i.e., pyridinic and quaternary N sites), whereas the less efficient 2 e^- pathway occurred on the in-plane N defects.[139] A number of NGR and CNT-based ORR catalysts have been reported by tuning their N sites and 3D architecture, such as pyridinic functionalized NWCNT,[140] NGR unzipped from CNT,[141] porous NGR,[142,143] NGR/CNT composite.[144]

Direct pyrolysis of carbon sources that are rich of nitrogen-containing groups is a facile method in producing N-doped carbons, some of which have been found to be active for ORR. Some proved nitrogen-rich carbon sources that can be used for ORR application include folic acid,[145] sugar/urea mixture,[146] and gelatin,[147] among others. By calculating the π and σ states of NC derived from gelatin/Ketjenblack carbon, Cho et al. found the graphitic-like N doping increased the metallic density of state at the Fermi level and the pyridine-like N doping increased the π states of carbon. A proper combination of graphitic and pyridinic N sites was proposed to facilitate the formation of $O_{2,ad}^-$ (reaction 17). A zinc−air battery employing the composite catalyst attained a maximum power density (P_{max}) of 193 mW cm^{-2}, cf. 188 mW cm^{-2} of the battery using Pt/C.[147] A primary zinc−air battery using the N-doped carbon nanofiber derived from coconut-based bacterial cellulose exhibited a discharge plateau at 1.34 and 1.25 V at the current densities of 1 and 10 mA cm^{-2}, respectively.[127] Zinc−air battery is a type of metal−air battery that uses metallic zinc as the anode, with a theoretical cell voltage of 1.65 V and a specific energy of 1353 Wh kg^{-1}. In practice, the open circuit voltage (OCV) of the zinc−air battery is around 1.50 V, with a specific energy of 370 Wh kg^{-1}.[148] Mesoporous N-doped nanocarbons could be derived from suitable templates or frameworks.[149−151] Figure 13 shows electrochemical performance of NC nanosheets derived from soft silica template. It exhibited impressive ORR performance with E_{onset} the same as Pt/C and $E_{1/2}$ 50 mV more positive than Pt/C (Figure 13d).[150] A metal-free N-doped porous carbon was derived from a composite of ZIF-7 framework [$Zn(PhIM)_2{\cdot}(H_2O)_3$; PhIM = benzimidazole] and glucose. The high porosity and surface area (783 $m^2\ g^{-1}$) was one of the reasons for the good ORR activity of the nanoporous carbon material.[151]

Boron is an electron-deficient dopant for carbon materials. Based on a combined experimental and density functional theory (DFT) calculation, Ma and Hu et al. proposed the following mechanism of B-doped CNTs.[152] Positively charged B dopant induced chemisorption of O_2 on B-doped CNTs. Some π^* electrons accumulated around the B dopant, which can be easily transferred to the chemisorbed O_2 for ORR with boron as a bridge. The mechanism was still valid when the B dopant was in oxidized states such as BC_2O, BCO_2, and so forth. Intuitively, the O_2 adsorption on B-doped carbons should be quite easy owing to the electron-deficiency around B sites and the considerable difference of electronegativity between B and O. Doped carbons with sole doping of B, however, exhibited rather modest activity for ORR.[152] To improve the ORR performance, B and N were used together as dopants for carbon. Dai et al. reported the synergetic effect of B- and N-doped vertically aligned CNTs and graphene on improving the ORR activity.[153,154] Chen et al. synthesized B- and N-codoped nanodiamond (BND) via microwave plasma enhanced chemical vapor deposition. A zinc−air battery using BND delivered 24.8 mW cm^{-2}, cf. 22.4 mW cm^{-2} of Pt/C.[155] Tour and Ajayan et al. synthesized B- and N-containing carbon nanoribbons (BNC-NR) that attained −0.03 V vs Ag/AgCl,[156] a better ORR catalyst than B- and N-doped graphene quantum dots/graphene hybrid reported by the same group.[157] Yang and Hu investigated two types of B- and N-doped CNTs, where one was dominated by bonded B−N sites and the other had separated B and N sites.[158] The experimental and DFT results showed that the B−N bonded CNT cannot, although the separated B- and N-doped CNT can, create the ORR activity. The reason for the inertness of B−N bonded CNT was that the long-pair electrons of N were largely neutralized by the vacant B dopant, and few electrons or vacant orbitals were left to conjugate with the carbon π system of CNT. In contrast, the separation of B from N of B−N doped CNT prevented the electronic neutralization between N, an electron donor, and B, an electron acceptor.[158] Those results explained the discrepancy of ORR activities of various B- and N-containing carbon materials and highlighted the importance of electrical neutralization degree between B and N on determining the ORR performance.

Sulfur has a close electronegativity to carbon and has been used as a dopant for carbon materials. An S-doped graphene was obtained by direct annealing of GO and benzyl disulfide (BDS).[159] Generally, the ORR activity of S-doped carbon is relatively low and it is more practical to have N- and S-codoped (NS) carbon, such as NS-doped graphene,[160,161] NS-doped CNT,[162] and NS-doped carbon black.[163] A type of mesoporous NS graphene was obtained by using melamine and BDS as the N and S sources, respectively, and colloidal silica as the

DOI: 10.1021/acscatal.5b00524
ACS Catal. 2015, 5, 4643−4667

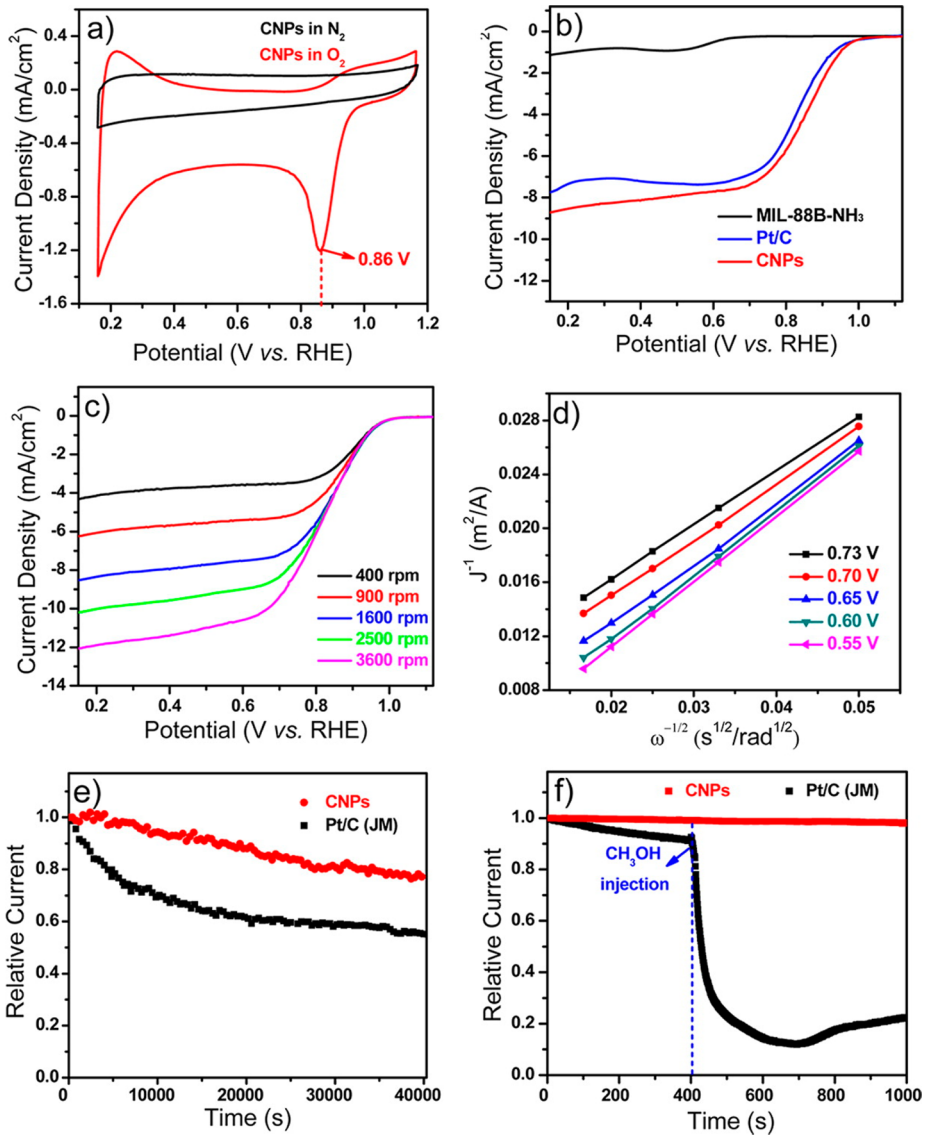

Figure 14. (a) CV curves of carbonized nanoparticles (CNPs) in N_2-saturated and O_2-saturated solution with 0.1 M KOH at a scan rate of 5 mV/s; (b) LSV curves of MIL-88B-NH3 NPs, CNPs, and Pt/C at a rotation rate of 1600 rpm; (c) LSV curves of CNPs in O_2-saturated 0.1 M KOH with various rotation rates at a scan rate of 5 mV/s; (d) Koutecky–Levich plots of CNPs derived from LSV curves at different electrode potentials; (e) chronoamperometric responses at 0.84 V in O_2-saturated 0.1 M KOH at CNP or Pt/C electrodes (1600 rpm) for 40000s; (f) chronoamperometric responses at 0.84 V in O_2-saturated 0.1 M KOH at CNP or Pt/C electrodes (1600 rpm) before and after addition of 2 M methanol. Note that the catalyst loading used in all electrochemical measurements is 0.39 mg/cm^2 for both CNPs and commercial Pt/C.[178]

structural template.[164] P and F are examples of less popular dopants of carbon as compared to N, B, and S. Some examples reported in literature include P-doped carbon hollow spheres,[165] N–P-doped biocarbon,[166] N–P–B-doped carbon black,[167] and F-doped carbon black.[168] The ORR performance of various nonmetal-doped carbon catalysts is listed in Table 2.

It is worth noting that the good ORR activity of nonmetal-doped carbons synthesized in the presence of metallic species should not be overestimated. For the example of heteroatom-doped graphene, graphene synthesized from graphite flakes by the Hummer's method had trace metal impurities, such as Mn, Fe, Ni, and Co. Pumera et al. argued the high possibility of metallic impurities in rendering the oxygen electrocatalysis of those claimed "metal-free" electrocatalysis in literature.[169] Although a cooperative role of metal impurities cannot be definitively ruled out in some nonmetal-doped carbons as mentioned above, it is worthwhile to emphasize that the ORR activity of nonmetal-doped carbons synthesized without the involvement of metallic species is essentially ascribable to the nonmetal doping effect.

3.2.2. Carbon–Transition Metal Hybrid. Carbon materials integrated with nitrogen and TM represent another group of ORR catalysts that are both active in aqueous solutions. Although not ruling out the catalytic role of TM (e.g., Fe and Co), Yeager and Wiescener independently thought that TM mainly served to facilitate the incorporation of N into carbon framework.[170,171] Their argument has been supported by the fact that the ORR activity was merely affected by the nature of precursors containing nitrogen, TM and carbon,[172,173] nitrogen content,[174] and TM content for the example of Fe-doped N-CNT (9 to 16 wt % Fe).[60] The argument is, however, challenged by the mechanistic study and recent experimental results. Wiggins-Camacho and Stevenson proposed a dual-site reaction mechanism of ORR on Fe-doped N-CNT, in which O_2

DOI: 10.1021/acscatal.5b00524
ACS Catal. 2015, 5, 4643–4667

was reduced to HO_2^- ($2e^-$ pathway, reaction 2) on N-CNT surfaces but the generated HO_2^- underwent rapid chemical disproportionation on Fe_xO_y/Fe surfaces.[60] The finding underlies the nontrivial role of TM species of carbon-transition metal hybrids. Furthermore, recent works have found the choice of nitrogen precursors, TM content, carbon support, and pyrolysis temperature greatly influences the activity of the carbon-transition metal hybrid catalysts.[174−177]

Composite materials consisting of C, N and Fe (Fe/N/C) are the most studied carbon-transition metal hybrid catalysts. Figure 14a−d, e, and f show the ORR activity, durability test and methanol tolerance test of a Fe/N/C catalyst derived from the pyrolysis of MIL-88B-NH_3 [$Fe_3O(H_2N\text{-}BDC)_3$, H_2N-BDC = 2-aminoterephtalic acid]. The salient performance was ascribed to the maximized sp^2 carbon, which had better conductivity than sp^3 carbon, and the rich of quaternary N, which possessed higher ORR activity compared with pyridine N.[178] An ADMFC using a carbon back containing N and trace Fe reached P_{max} of 22.7 mW/cm^2, 1.7 times higher than that of commercial Pt/C.[179] Cho and Liu et al. created a tetrapod structured Fe/N/C composite catalyst derived from α-Fe/Fe_3C-functionalized melamine foam and N-doped Ketjen Black. Xu et al. investigated Fe−N_x/C catalysts from Black Pearls 2000 and $FeCl_3$ and reported the following order of ORR activity: FeN_2−C ≈ FeN_4−C > Fe_4−N−C > N−C ≫ Fe_4−C ≈ C.[180] It is worth noting that Fe/N/C catalysts can be easily prepared from direct pyrolysis of mechanically mixed or polymeric precursors,[181−188] so that low-cost and scalable manufacturing of Fe/N/C catalysts is technically viable. This shows great potential of Fe/N/C catalysts for large-scale industrial applications.

Co is another popular transition metal for a carbon−transition metal hybrid catalyst for ORR, after the discovery of cobalt phthalocyanine and pyrolysis of transition-metal macrocycles in the 1960s.[189] The same as Fe/N/C, Co is mostly used together with N as dopant for carbon. Recent development of carbon catalysts doped with Co and N (Co/N/C) includes mesoporous Co/N/C hybrid,[190] Co/N/C hollow spheres,[191] and Co/N/rGO[192] Generally, the ORR activity of Co/N/C is inferior to Fe/N/C. Table 3 lists the ORR performance of various carbon-transition metal hybrid catalysts.

3.3. Transition Metal Oxides. *3.3.1. Spinel.* Spinel, in general formulation of AB_2O_4, has the oxide anions arranged in a cubic close-packed lattice, where 1/8 of the tetrahedral sites are occupied by A atoms, and 1/2 of the octahedral sites are occupied by B atoms. Pure transition metal spinel oxides are relatively inert toward ORR, albeit a good OER catalyst in basic solutions.[193] In 2011, the Dai group revealed that Co_3O_4 nanoparticles grown on N-doped reduced mildly oxidized graphene oxide (N-rmGO) exhibited superb activity for ORR, besides OER, in alkaline media.[194] After that seminal work, extensive studies for spinel/nanocarbon hybrid were carried out, where the transition metal spinel oxides at least include Co_3O_4,[195−197] $MnCo_2O_4$,[198−200] $NiCo_2O_4$,[201−204] $FeCo_2O_4$,[205,206] $CuCo_2O_4$,[207] $CoFe_2O_4$,[206,208,209] Fe_3O_4,[210−212] $CoMn_2O_4$,[198,213−215] $ZnMn_2O_4$,[213] Mn_3O_4,[216−219] and various heterogeneous nanostructures based on these spinel oxides.[220−224]

Co_3O_4 is of normal spinel structure and is a p-type seminconductor with the fundamental band gap of 0.74 eV. The small band gap of Co_3O_4 is due to a direct dipole-forbidden d−d transition between tetrahedral-site Co^{2+} cations.[225] In Dai's seminal work, E_{onset} and $E_{1/2}$ of Co_3O_4/N-rmGO was 0.93 and 0.82 V, respectively. The measured HO_2^- of Co_3O_4/N-rmGO was below 6%, and a gas-diffusion layer loaded with Co_3O_4/N-rmGO exhibited negligible degradation in 0.1 M KOH solution.[194] Slightly inferior performance was evident when the N-rmGO was replaced by CNT,[226] rGO,[227] mesoporous carbon,[228] and N-doped carbon.[196] The good ORR activity of Co_3O_4/N-rmGO was attributed to the synergetic covalent coupling between Co_3O_4 and N-rmGO, as well as the unique property of N-rmGO. Wang and Zhou et al. investigated the chemical, electronic, and structural nature of Co_3O_4/N-rmGO by scanning transmission X-ray microscopy (STXM) through spatially resolved X-ray absorption near edge structure (XANES) spectroscopy and chemical imaging.[229] Besides the carbon and oxygen sites on graphene, N-sites on graphene were the major anchoring sites for Co_3O_4. Co_3O_4 nanocrystals were partially reduced via $Co^{3+}(O_h)$ to $Co^{2+}(O_h)$ and the reduction varied spatially on and among individual Co_3O_4 nanocrystals. Xiao and Yang et al. studied the influence of surface structures of Co_3O_4 on ORR. Three types of Co_3O_4 nanocrystals were synthesized (i.e.,

Table 3. ORR Performance of Transition Metal−Carbon Hybrid Catalysts Obtained from RDE[a]

catalysts	E_{onset} vs RHE[b] $E_{1/2}$ vs RHE	durability/remarks	ref
iron-based			
Fe/Fe_3C/N/C	0.98[***] 0.87[***]	62% retention of j under 0.81 V for 5.6 h	182
Fe/N_x/C	1.05 0.87		180
Fe/N/C	1.03 0.82	79% retention of j under 0.84 V for 11 h	178
Fe/N/C	0.92 0.81		183
Fe/$Fe_{2.5}C$/N/C	0.90 0.72	42 mV penalty of $E_{1/2}$ after 5000 cycles from 1.0 to 0.6 V	185
Fe_3C/N/CNT	0.96 0.83	negligible degradation of E_{onset} and j_L after 3000 cycles from 0.96 to 0.36 V	184
Fe_xC/NGR	0.98[***] 0.86[***]	30 mV penalty of $E_{1/2}$ after 2000 cycles from 0.94 to 0.68 V	186
FeN/Fe_2N/NGR	0.92[**] 0.78[**]	91% retention of j under 0.71 V for 5.6 h	187
FeS/Fe_3C/Fe_2C/N/C	0.92 0.78	97% retention of j under 0.57 V for 5 h	181
FeP/Fe_2P/$Fe_2P_2O_7$/C	0.86 undefined	87% retention of j under 0.63 V for 12 h	188
cobalt-based			
Co/N/C	0.90 0.77	9 mV penalty of $E_{1/2}$ after 10 000 cycles from 1.0 to 0.6 V	190
Co/N/C	0.84[**] 0.65[**] (1900 rpm)	90% retention of j for 2.8 h	191
Co/N/rGO	0.83 undefined	80% retention of j under 0.66 V for 6 h	192

[a]The rotating rate of RDE is 1600 rpm, and the electrolyte is O_2-saturated 0.1 M KOH/NaOH, unless otherwise stated. [b]: η_{onset} is readily calculated from E_{onset} by η_{onset} = 1.227 V − E_{onset}. [*]: converted from Ag/AgCl in 3 M KCl, $E_{vs\ RHE} = E_{vs\ Ag/AgCl}$ + 0.209 V + 0.059 × pH. [**]: converted from Ag/AgCl in saturated KCl, $E_{vs\ RHE} = E_{vs\ Ag/AgCl}$ + 0.197 V + 0.059 × pH. [***]: converted from saturated camel electrode, $E_{vs\ RHE} = E_{vs\ SCE}$ + 0.241 V + 0.059 × pH. [****]: converted from Hg/HgO electrode, $E_{vs\ RHE} = E_{vs\ MMO}$ + 0.098 V + 0.059 × pH.

DOI: 10.1021/acscatal.5b00524
ACS Catal. 2015, 5, 4643−4667

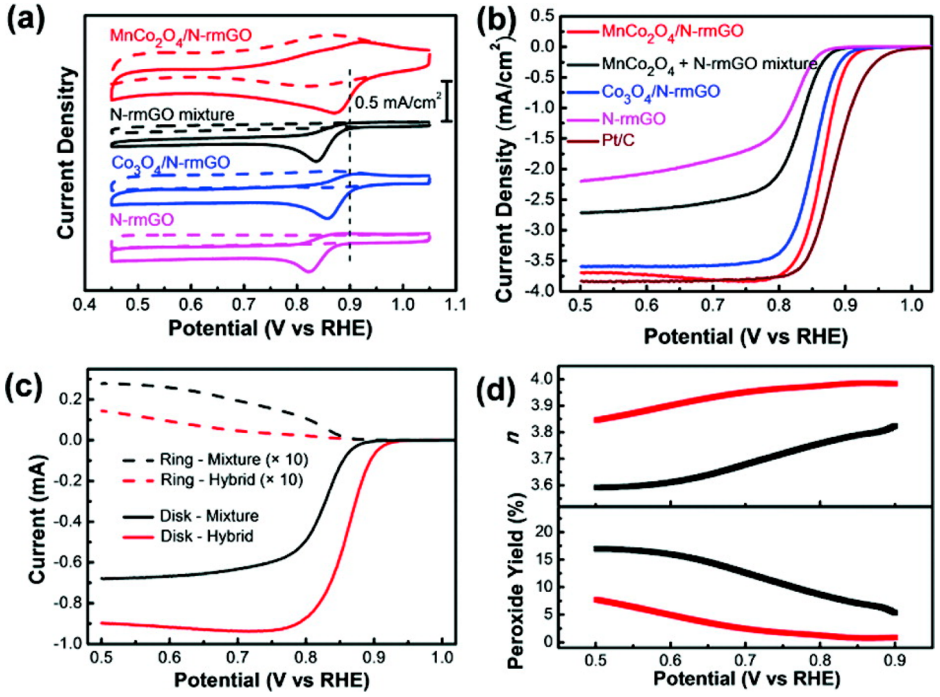

Figure 15. (a) CV curves of $MnCo_2O_4$/N-rmGO hybrid, $MnCo_2O_4$ + N-rmGO mixture, Co_3O_4/N-rmGO hybrid, and N-rmGO on glassy carbon electrodes in O_2-saturated (solid line) or N_2-saturated (dash line) 1 M KOH. The peak position of Pt/C was shown as a dashed line for comparison. (b) Rotating-disk electrode voltammograms of $MnCo_2O_4$/N-rmGO hybrid, $MnCo_2O_4$ + N-rmGO mixture, Co_3O_4/ N-rmGO hybrid, N-rmGO, and Pt/C in O_2-saturated 1 M KOH at a sweep rate of 5 mV/s at 1600 rpm. (c) Rotating ring−disk electrode voltammogram of $MnCo_2O_4$/N-rmGO hybrid and $MnCo_2O_4$ + NrmGO physical mixture in O_2-saturated 1 M KOH at 1600 rpm. The disk potential was scanned at 5 mV/s, and the ring potential was constant at 1.3 V vs RHE. (d) Percentage of peroxide (bottom) with respect to the total oxygen reduction products and the electron transfer number (n) (top) of $MnCo_2O_4$/N-rmGO hybrid (red lines) and $MnCo_2O_4$ + N-rmGO mixture (black lines) at various potentials based on the corresponding RRDE data in panel c. Catalyst loading was 0.10 mg/cm^2 for all samples.[233]

(110)-terminated nanorods, (100)-terminated nanocubes, and (111)-terminated nano-octahedrons). The ORR activity of the faces of Co_3O_4 was known as (111) > (100) > (110). This ranking of ORR activity correlated very well with the surface Co^{2+} density of the facets of Co_3O_4. A high surface Co^{2+} density resulted in good ORR activity of Co_3O_4 nanocrystals.[230] Besides Co_3O_4/nanocarbon hybrids, metallic Co was incorporated together with Co_3O_4 and nanocarbon in order to mitigate the low conductivity problem of Co_3O_4, such as Co/Co_3O_4/N/C composite,[223] and core−shell Co@Co_3O_4/bamboo-like N-doped CNTs (BNCNTs).[220]

Hausmannite Mn_3O_4 is of spinel structure. A hybrid catalyst consisting of 37 nm Mn_3O_4 particles and NrGO showed almost equivalent catalytic activity to commercial Pt/Vulcan and the ORR favored the 4e$^-$ pathway on Mn_3O_4/NrGO surfaces.[231] Gao et al. reported a dicyandiamide-mediated growth of $MnCO_3$ and the following reduction of $MnCO_3$ by N-doped carbon during pyrolysis.[217] The resulted Mn_3O_4 nanorods were uniformly coated by a layer of N-doped carbon with thickness of 5 nm. Sun et al. reported a composite of Ag−Mn_3O_4−C for ORR and zinc-air battery using the composite catalyst.[120] Wang et al. synthesized Ag−Mn_3O_4 nanoparticles on Vulcan carbon black.[216] The initial growth of Mn_3O_4 on Vulcan catalyzed the anchoring of Ag adjacent to Mn_3O_4. In comparison with Ag/C, Mn_3O_4/C, and Ag/Mn_3O_4/C blend, Ag−Mn_3O_4/C hybrid exhibited improved ORR activity because of the covalent coupling between Ag and Mn_3O_4 and the oxygen spillover effect from Ag_2O/Ag to Mn_3O_4, as systematically investigated by XANES, X-ray photoelectron spectroscopy (XPS), and cyclic voltammetry (CV).[216] Oxygen spillover is a concept in heterogeneous catalysis and electrocatalysis. Oxygen atoms could adsorb and dissociate on the surfaces of Ag_2O/Ag. The migration of these adsorbed oxygen atoms from Ag_2O/Ag to Mn_3O_4 comprises the oxygen spillover phenomenon. The oxygen spillover concatenates the reaction paths of ORR on two or more catalyst surfaces, which would be otherwise not possible on a single catalyst surfaces. Therefore, oxygen spillover plays a constructive role for ORR.

Magnetite Fe_3O_4 has a cubic inverse spinel structure where Fe^{2+} cations occupy half of the octahedral sites and Fe^{3+} cations occupy the other half of octahedral sites and all the tetrahedral sites. A number of Fe_3O_4-based catalysts have been reported for the ORR, such as 3D Fe_3O_4/NGR,[212] Fe_3O_4/N-doped carbon,[211] Fe_3O_4−Co_3O_4 yolk−shell nanostructure,[224] and Co/Fe_3O_4.[221]

Mn−Co spinel oxides, with the formulation $Mn_xCo_{3-x}O_4$, were explored for ORR applications, noting that Mn cations are completely miscible with Co cations in spinel structure. $Mn_xCo_{3-x}O_4$ could be synthesized by various methods (e.g. organic precipitation,[232] inorganic coprecipitation,[213] solvothermal,[233] hydrothermal,[200] sol−gel,[234,235] microwave heating,[236] combustion,[237] and polyol-based precursor route[238]). Recently, Chen et al. reported a rapid reduction-recrystallization method to form nanocrystalline Mn−Co spinel from amorphous MnO_2 at room temperature.[205] Dai et al. synthesized $Mn_xCo_{3-x}O_4$/N-rmGO with varied Mn/Co ratio. The $Mn_xCo_{3-x}O_4$ (x = 1, $MnCo_2O_4$)/N-rmGO showed higher ORR current density than $Mn_xCo_{3-x}O_4$ (x = 0.6)/N-rmGO, $Mn_xCo_{3-x}O_4$ (x = 1.5)/N-rmGO, $Mn_xCo_{3-x}O_4$ (x = 2)/N-rmGO, and $Mn_xCo_{3-x}O_4$ (x = 3)/N-rmGO. $MnCo_2O_4$/N-rmGO exhibited the same E_{onset}

DOI: 10.1021/acscatal.5b00524
ACS Catal. 2015, 5, 4643−4667

Table 4. ORR Performance of Spinel Catalysts Obtained from RDE[a]

catalysts	E_{onset} vs RHE[b] $E_{1/2}$ vs RHE	Tafel slope (mV/decade)	durability/remarks	ref
simple spinel				
Co_3O_4/N-rmGO	0.93 0.82	−42		194
Co_3O_4/rGO	0.90* 0.79*		96% retention of j under 0.41 V for 1.7 h	227
Co_3O_4/rGO	0.89*** 0.68***	−101	98% retention of j under 0.47 V for 2.8 h	230
Co_3O_4/N/C	0.92 0.79		92% retention of j for 10 h	196
Co@Co_3O_4/NCNT	0.92**** 0.76****	−83	78% retention of j under 0.47 V for 5.6 h	220
Co/Co_3O_4/N/C	0.81**** undefined			223
Mn_3O_4/NrGO	1.05*** 0.71***		10 mV penalty of $E_{1/2}$ after 3000 cycles from 1.21 to 0.21 V	231
Mn_3O_4/N/C	0.91**** undefined		94% retention of j under 0.57 V for 4.2 h	217
Mn_3O_4/Ag/C	0.96*** 0.85*** (1 M NaOH)	−60 (low j); −120 (high j)		216
Mn_3O_4/Ag/C	0.87**** 0.69****		35 mV penalty of $E_{1/2}$ after 2000 cycles from 0.97 to 0.37 V	120
Fe_3O_4/NrGO	0.86** undefined**			212
Fe_3O_4/N/C	0.92* 0.76*		90% retention of j under 0.56 V for 2.8 h	211
Fe_3O_4/Co_3O_4	0.84** 0.65**		44% retention of j for 1 h	224
Fe_3O_4 /Co/C	0.90 undefined		97% retention of j under 0.76 V for 2.8 h	221
complex spinels				
$MnCo_2O_4$/N-rmGO	0.93 0.85		96% retention of j under 0.70 V for 5.6 h	233
$Mn_{0.4}Co_{2.6}O_4$/C	0.88 0.75		86% retention of j under 0.47 V for 2.8 h	198
$MnCo_2O_4$/CNT	1.03** 0.70**		87% retention of j under 0.66 V for 90 h	199
$CoMn_2O_4$/C	0.90** 0.67**		96% retention of j under 0.46 V for 3.3 h	213
$NiCo_2O_4$	0.79 undefined		50 mV penalty of E_{onset} after 1000 cycles	243
$NiCo_2O_4$	0.89* 0.75*		70% retention of j under 0.67 V for 100 h	204
$NiCo_2O_4$/rGO	0.87 undefined			202
$NiCo_2O_4$/NrGO	0.88*** 0.64***		87% retention of j under 0.71 V for 2 h	201
$CuCo_2O_4$/NrGO	0.89*** 0.78***		85% retention of j under 0.71 V for 5.6 h	207

[a]The rotating rate of RDE is 1600 rpm, and the electrolyte is O_2-saturated 0.1 M KOH/NaOH, unless otherwise stated. [b]: η_{onset} is readily calculated from E_{onset} by $\eta_{onset} = 1.227\ V - E_{onset}$. *: converted from Ag/AgCl in 3 M KCl, $E_{vs\ RHE} = E_{vs\ Ag/AgCl} + 0.209\ V + 0.059 \times pH$. **: converted from Ag/AgCl in saturated KCl, $E_{vs\ RHE} = E_{vs\ Ag/AgCl} + 0.197\ V + 0.059 \times pH$. ***: converted from saturated camel electrode, $E_{vs\ RHE} = E_{vs\ SCE} + 0.241\ V + 0.059 \times pH$. ****: converted from Hg/HgO electrode, $E_{vs\ RHE} = E_{vs\ MMO} + 0.098\ V + 0.059 \times pH$.

with Co_3O_4/N-rmGO and 30 mV more positive $E_{1/2}$ than Co_3O_4/N-rmGO (Figure 15). Particle sizes less than 5 nm and optimized range of $MnCo_2O_4$ between 65 and 80 wt % were crucial for the good ORR performance of $MnCo_2O_4$/N-rmGO.[233] In contrast to a stoichiometric Co^{2+}/Co^{3+} ratio of 1:2 of Co_3O_4/N-rmGO, the Co^{2+}/Co^{3+} ratio of $MnCo_2O_4$/N-rmGO is above 1:2, and XANES results suggested Mn cations were mainly Mn^{3+} in coexistence with a small amount of Mn^{4+}. The formula of $MnCo_2O_4$ was, therefore, described to be $Co^{2+}(Co^{3+}Mn^{3+})O_4$. Liu et al. reported a dual-phase $MnCo_2O_4$ comprising 77 wt % of cubic $(Mn_{1/3}Co_{2/3})[Mn_{1/3}Co_{2/3}]_2O_4$ and 23 wt % of tetragonal $(Co,Mn)[Mn,Co]_2O_4$.[200] The Mn^{3+}/

DOI: 10.1021/acscatal.5b00524
ACS Catal. 2015, 5, 4643−4667

Mn^{4+} redox couples located at the octahedral sites (i.e., B-site of AB_2O_4) were generally considered as the active sites for ORR and were more active than the Co species.[239−241] Kwon et al. investigated the composition effects of a composite of $Mn_xCo_{3-x}O_4$ (x = 0, 0.4, 0.8, 1.4, 1.9, and 3) and Ketjen Black. The substituted Mn in $Mn_xCo_{3-x}O_4$ was found to be mainly as Mn^{3+} and in the octahedral site. The highest ORR activity was observed with $Mn_{0.4}Co_{2.6}O_4$.[198] Qiao et al. reported a room temperature synthesis of $MnCo_2O_4$ based on a solvent−nonsolvent route using metal chlorides and KOH.[199] A composite catalyst consisting of 80 wt % CNT and 20 wt % the highly defective and poorly crystalline $MnCo_2O_4$ showed a relatively positive E_{onset} of 0.07 V vs Ag/AgCl. Chen et al. synthesized $CoMn_2O_4$ from a coprecipitation method using NaOH as the precipitating agent. The $CoMn_2O_4$(30 wt %)/Vulcan composite catalyst showed modest ORR activity.[213]

$NiCo_2O_4$ is a semiconductor with electronic transport based on the variable-range hopping and nearest-neighbor hopping mechanisms.[242] Su and Chen et al. reported a hydrothermal synthesis of urchin-like $NiCo_2O_4$ spheres.[243] Cao et al. prepared a 3D macroporous cubic spinel $NiCo_2O_4$, consisting of numerous $NiCo_2O_4$ nanoparticles in size of 20−40 nm that further aggregated into slabs with thickness of 150 nm. The macroporous structure, with pore volumes of 0.23 $cm^3\ g^{-1}$, enabled facile mass transport of reactants to the active surface sites. The macroporous $NiCo_2O_4$ catalysts exhibited good ORR activity with E_{onset} of 0.89 and $E_{1/2}$ of 0.75 V.[204] Lou et al. developed a polyol synthesis of $NiCo_2O_4$−rGO hybrid by refluxing metal acetates with ethylene glycol and subsequent annealing at a temperature as low as 300 °C.[202] $NiCo_2O_4$/NrGO and $CuCo_2O_4$/NrGO synthesized by hydrothermal methods using NH_4OH as the precipitating and N-doping agent were also reported.[201,207] The ORR performance of various simple spinel and complex spinel catalysts is listed in Table 4.

3.3.2. Perovskite. Perovskite (ABO_3) consists of corner-shared BO_6 octahedra together with A-site cations at the corner of the unit cell. The perovskite structure is flexible and robust and can withstand considerable lattice mismatch between the (A−O) and (B−O) bond lengths and accommodate versatile dopants on A-site and/or B-site lattices. This unique structure confers some perovskite with good ORR, OER,[244−248] and bifunctional ORR/OER activity.[249−256] Section 3.3.2 only reviews those perovskite oxides solely for ORR.

The works on perovskite for ORR dated back to 1970s, where Matsumoto et al. reported $LaNiO_3$ for oxygen electrocatalysis.[257,258] Investigating 18 substituted perovskites $La_{1-x}Sr_xTMO_3$ (TM = Ni, Co, Mn, Fe, Cr, and V), Bockris and Otagawa found an increase of the catalytic activity of perovskites occurred in parallel with a high occupancy of antibonding σ^* orbitals of TM−OH, and they proposed a volcano plot of catalytic activity versus TM−OH bond strength.[259] La-based perovskite was found to be of best ORR activity among $LnMnO_3$ (Ln = rare earth metals), in the series of La > Pr > Nd > Sm > Gd > Y > Dy > Yb.[260] For the alkaline earth doping effect on the A-site, half-cell testing on catalyst-loaded gas-diffusion electrodes showed the series of $Pr_{0.8}Sr_{0.2}MnO_3$ > $Pr_{0.8}Ca_{0.2}MnO_3$ > $Pr_{0.8}Ba_{0.2}MnO_3$ > $PrMnO_3$, and all the catalysts were free of impurity phases after 200 h of testing in 8 M KOH solution.[261] ORR on perovskite surfaces is complicated and depends on its intrinsic activity, electronic conductivity, surface absorption behavior, and the incorporation of conducting additives. Sunarso et al. reported the intrinsic ORR activity of $LaTMO_3$ (TM = Ni, Co, Fe, Mn, and Cr) ranked in the order of $LaCoO_3$, $LaMnO_3$, $LaNiO_3$, $LaFeO_3$, and $LaCrO_3$, without the addition of carbon blacks. The formation of HO_2^- was as low as 1.5%, indicating a pseudo $4e^-$ pathway.[262] In contrast, it was stated that Co-based perovskite oxides were less active than Mn-based ones.[53] Huang et al. reported the n value of ORR of $LaMnO_3$ was 2.95, indicating a slightly more prevalent $2e^-$ pathway.[263] For $LaNi_{0.5}M_{0.5}O_3$, the ORR kinetics was enhanced in the order of $LaNi_{0.5}Fe_{0.5}O_3$, $LaNi_{0.5}Co_{0.5}O_3$, $LaNi_{0.5}Cr_{0.5}O_3$, $LaNi_{0.5}Mn_{0.5}O_3$, with 2% of the yield of HO_2^-.[262] It is worth noting that the exact reaction pathways of bare $LaMO_3$ without conducting additives are still under debate. While most studies focus on powdered catalysts, Shao-Horn et al. investigated epitaxially oriented $La_{1-x}Sr_xMnO_3$ surfaces on Nb-doped $SrTiO_3$ substrates for ORR. They found the activity was greatest for $La_{0.67}Sr_{0.33}MnO_3$, but the (110) and (111) orientations displayed comparable activity to that of the (001).[264]

For those perovskite with low electronic conductivity, the addition of conducting agents, such as carbon blacks, helps to supply electrons from the electrode to the perovskite surface during ORR. After coupling the addition of $LaNiO_3$ with 17 wt % acetylene black (AB), Shao-Horn et al. found the area-specific and mass-specific activity of $LaNiO_3$ were better than $La_{0.75}Ca_{0.25}FeO_3$ and $LaCu_{0.5}Mn_{0.5}O_3$.[265] The group later reported a volcano plot for the ORR activity of perovskite oxides mixed with acetylene black, in the series: $LaMnO_{3+\delta}$ > $LaNiO_3$ > $La_{0.5}Ca_{0.5}MnO_3$ > $LaMnO_3$ > $LaMn_{0.5}Ni_{0.5}O_3$ > $La_{0.5}Ca_{0.5}CoO_{3-\delta}$ > $La_{1-x}Ca_xFeO_3$ > $La_{1-x}Ca_xCrO_3$ (Figure 16).[65] Good activity for ORR was observed in $LaMnO_3$/carbon composites, such as $LaMnO_3$/CNF and $LaMnO_3$/Vulcan.[266,267] The underlying principle for enhancing the ORR activity of perovskite oxides is that an e_g-electron ~1 as well as the increased covalency between transition metal 3d and O 2p orbitals.[65] As an example of $LaCoO_3$, the yield of HO_2^- was as high as 50% for bare $LaCoO_3$, and a pseudo $4e^-$ pathway was only attained by the mixing of carbon blacks with $LaCoO_3$.[268] A similar $2e^-$ + $2e^-$ pathway was observed for $La_{0.6}Ca_{0.4}CoO_3$/C composite in 1 M KOH, with ca. 3% of HO_2^- production during ORR.[269] For barium strontium cobalt iron perovskite oxides (BSCF), the HO_2^- formation during ORR was in the range from 50 to 60%.[270] The argument was further confirmed by the substantial reduction current emerged from Ar-saturated 0.1 M KOH + 2 mM HO_2^- electrolyte. The BSCF/AB composite showed improved E_{onset} and reduced HO_2^- formation as compared to bare BSCF. The optimized BSCF/AB composite, BSCF(78 wt %)/AB, exhibited 28% HO_2^- formation and n value of 3.43 during ORR.[271] Despite the fact that carbon blacks were not efficient for ORR, mixing it with perovskite oxides led to a strong drop of the HO_2^- formation. A study of channel flow cell indicated that most of the O_2 was reduced via the $2e^-$ pathway on $La_{0.6}Ca_{0.4}CoO_3$ (LCC)−Vulcan carbon composite. The generated HO_2^- appeared to be stable at Vulcan carbon and was further reduced and/or chemically decomposed on LCC surfaces.[272] On the basis of the above results, the ORR on poorly conducting perovskite/carbon composites was known to proceed through a $2e^-$ + $2e^-$ pathway, where OH^- was reduced to HO_2^- by carbon blacks and HO_2^- was further reduced to H_2O by perovskite oxides. In contrast, much less HO_2^- was observed on relatively conductive perovskite, such as $La_{0.8}Sr_{0.2}MnO_3$.[53,268] The performance of perovskite/carbon catalysts can be further improved by establishing perovskite/

DOI: 10.1021/acscatal.5b00524
ACS Catal. 2015, 5, 4643−4667

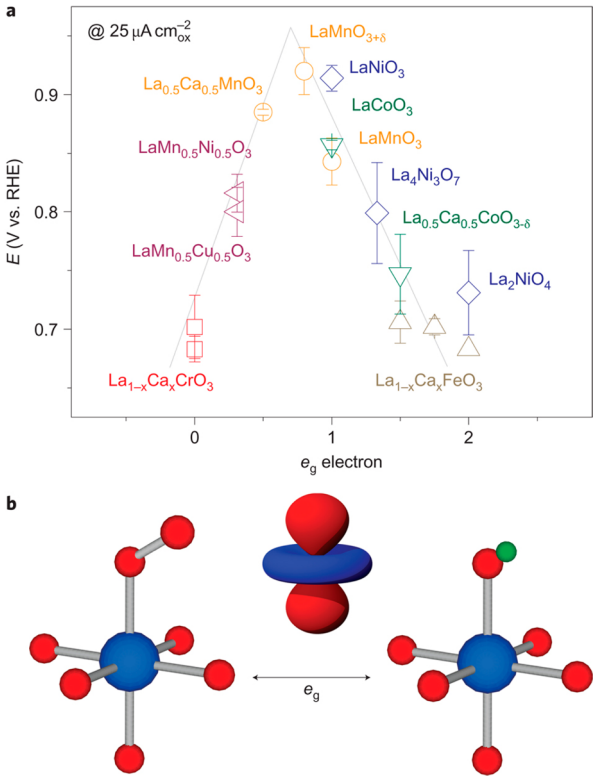

Figure 16. Role of e_g electron on ORR activity of perovskite oxides. (a) Potentials at 25 μA cm_{ox}^{-2} as a function of e_g orbital in perovskite-based oxides. Data symbols vary with type of B ions (Cr, red; Mn, orange; Fe, gray; Co, green; Ni, blue; mixed compounds, purple), where x = 0 and 0.5 for Cr, and 0, 0.25, and 0.5 for Fe. Error bars represent standard deviations. (b) The shape of the e_g electron points directly toward the surface O atom and plays an important role during O_2^{2-}/OH^- exchange. O, B, and H atoms are colored blue, red, and green, respectively. Reprinted with permission from ref 65. Copyright 2011 Nature Publishing Group.

carbon hybrids with certain interactions between the perovskite and carbons. For example, both the E_{onset} and $E_{1/2}$ are significantly improved by establishing a La-$(Co_{0.55}Mn_{0.45})_{0.99}O_3$/graphene hybrid than using La-$Co_{1-x}Mn_xO_3$/graphene mixture.[40,273] More works on perovskite/carbon hybrids should be carried out to fully leverage the good ORR activity of perovskite catalysts. The ORR performance of various perovskite catalysts is listed in Table 5.

3.3.3. Other Oxides. CoO is a metastable and thermodynamically less stable than Co_3O_4 at room temperatures. CoO is oxidized if stored in air for more than 1 year or immersed in O_2-saturated alkaline solution over 12 h.[274] It was reported that surface Co^{2+} was highly active for ORR.[230] Dai et al. reported CoO/NCNT hybrid with CoO loading between 50 and 67 wt % by a facile wet chemistry synthesis and low temperature annealing.[226] The CoO/NCNT hybrid exhibited E_{onset} of 0.93 V and $E_{1/2}$ of 0.86 V, and afforded higher oxygen reduction current density than Co_3O_4/N-rmGO. The salient activity of CoO/NCNT hybrid could be partly due to the higher electrical conductivity than that of Co_3O_4/N-rmGO. For the case of CoO/Vulcan carbon black catalysts, Jiang and Sun et al. found the turnover frequency (TOF) of the ORR per active CoO site is largely independent of the particle size in the range of 3 to 7 nm. The enhanced ORR activity for the smaller CoO particles was attributed to the enlarged interface between CoO and Vulcan.[274] P_{max} of zinc-air fuel cells followed the sequence of Pt/Vulcan (136 mW/cm^2) > CoO_x/oxidized-Vulcan (123 mW/cm^2) > CoO_x/amide-functionalized Vulcan (110 mW/cm^2) > CoO_x/Vulcan (100 mW/cm^2) > MnO_2/Vulcan (90 mW/cm^2).[275] Sophisticated Co-CoO-Co_3O_4/N/C hybrid derived from zeolitic imidazolate framework-9 (ZIF-9) exhibited similar catalytic activity to commercial Pt/Vulcan.[276]

Manganese oxides (MnO_x) have a long history as being ORR catalysts and have been widely used in primary batteries such as alkaline-MnO_2 cells, zinc-air battery, zinc−carbon cells, etc.[277] Ohsaka et al. reported that the ORR activity of different MnO_x followed the order: Mn_5O_8 < Mn_3O_4 < Mn_2O_3 < MnOOH.[278] MnO_2 has versatile polymorphs such as one-dimensional α-, β- and γ-MnO_2 and two-dimensional δ-MnO_2. The catalytic performance of MnO_2 was reported to follow the sequences: α-MnO_2> β-MnO_2> γ-MnO_2,[279] or α-MnO_2 ∼ δ-MnO_2 > λ-MnO_2 > β-MnO_2.[280] α-MnO_2 possesses a large tunnel structure which makes fast ion transport such as OH^- and related intermediates. Due to the relatively low electric conductivity of MnO_2, a lot of efforts have been committed to create MnO_2/carbon hybrid or composite materials. The α-MnO_2(50 wt %)−Vulcan composite was most active for ORR and zinc-air batteries among α-MnO_2−Vulcan composites.[281] A MnO_2 nanoflake with thickness of 1.5 nm was synthesized by a hot injection reaction between $KMnO_4$ and cetrimonium bromide (CTAB). The specific activity at 0.75 V could attain 21 mA mg^{-1}.[282] Li et al. reported the direct growth of δ-MnO_2 nanoflowers on rGO. The δ-MnO_2/rGO hybrid catalyst showed a dominant pseudo 4e$^-$ pathway for ORR and comparable performance with Pt/Vulcan.[283] MnO_x/graphene hybrids with good electrocatalytic behavior were also reported, ascribed to the synergistic coupling of NrGO and MnO_x.[284,285]

4. CONCLUDING REMARKS AND FUTURE CHALLENGES

Oxygen reduction reaction (ORR) is one of the most important and classic electrode reactions in electrocatalysis. It has been attracting great interests in recent years due to the large demand of green energy devices. Specifically, this review paper focused on ORR in alkaline media, which had fundamental influences on metal-air batteries, alkaline hydrogen fuel cells, alkaline direct alcohol fuel cells, microbial fuel cells, etc. Section 2.1 introduced the ORR thermodynamics and reaction kinetics, including the equilibrium potential of OH^-/H_2O redox couple, polarization curves, Tafel plots, RDE and RRDE. Sections 2.2 and 2.3 reviewed the reaction pathways of precious metal catalysts and transition metal oxide catalysts, respectively. Different reaction pathways in literature were categorized into three types, i.e. the 2 e$^-$ pathway, 4e$^-$ pathway and 2 e$^-$ + 2 e$^-$ pathway. Section 3 was devoted to the recent advances of catalysts for ORR, especially in the last three years. Section 3.1 reviewed Pt, Au, Pd and Ag-based catalysts. Section 3.2 reviewed carbon-based catalysts, including nonmetal-doped carbons and carbon- transition metal hybrid/composites. Section 3.3 reviewed transition metal oxide catalysts, namely spinel, perovskite, CoO and MnO_x. We did not cover other categories of ORR catalysts, such as transition metal macrocycles,[170,286−290] polymers,[291,292] metal nitrides,[293−298] chalcogenide,[299] and various composite/hybrids.[300,301] Some other ORR-related topics, such as the ORR catalysts in acidic, neutral and organic media, as well as bifunctional catalysts for both ORR and OER, were beyond the scope of this review paper.

Reaction mechanisms and pathways of precious metal-based ORR catalysts, in the forms of single crystals and carbon-

DOI: 10.1021/acscatal.5b00524
ACS Catal. 2015, 5, 4643−4667

Table 5. ORR Performance of Perovskite Catalysts Obtained from RDE[a]

catalysts	E_{onset} vs RHE[b] $E_{1/2}$ vs RHE	Tafel slope (mV/decade)	ref
$LaCoO_3$	0.88		262
	undefined		
$LaNiO_3$	0.72		
	undefined		
$LaNi_{0.5}Mn_{0.5}O_3$	0.81		
	undefined		
$La_{0.67}Sr_{0.33}MnO_3$ film	0.91		264
	undefined		
$Ba_{0.5}Sr_{0.5}Co_{0.8}Fe_{0.2}O_{3-\delta}$	0.73	−64	271
	undefined		
$Ba_{0.5}Sr_{0.5}Co_{0.8}Fe_{0.2}O_{3-\delta}$ (56 wt %)/acetylene black	0.84	−65	
	undefined		
$LaNiO_3$/C	0.95		265
	undefined		
$La_{0.6}Ca_{0.4}CoO_3$/C	0.92****	−66 (low j);	269
	undefined	−84 (high j)	
	(1 M KOH)		
$La_{0.8}Sr_{0.2}MnO_3$/C	0.95		268
	undefined		
	(1 M NaOH)		
$LaMn_{0.9}Co_{0.1}O_3$/GR	0.73*****		273
	0.49*****		

[a]The rotating rate of RDE is 1600 rpm, and the electrolyte is O_2-saturated 0.1 M KOH/NaOH, unless otherwise stated. [b]: η_{onset} is readily calculated from E_{onset} by $\eta_{onset} = 1.227\ V - E_{onset}$. *: converted from Ag/AgCl in 3 M KCl, $E_{vs\ RHE} = E_{vs\ Ag/AgCl} + 0.209\ V + 0.059 \times pH$. **: converted from Ag/AgCl in saturated KCl, $E_{vs\ RHE} = E_{vs\ Ag/AgCl} + 0.197\ V + 0.059 \times pH$. ***: converted from saturated camel electrode, $E_{vs\ RHE} = E_{vs\ SCE} + 0.241\ V + 0.059 \times pH$. ****: converted from Hg/HgO electrode, $E_{vs\ RHE} = E_{vs\ MMO} + 0.098\ V + 0.059 \times pH$.

supported nanocrystals, have been studied in an extensive manner for decades. Reaction mechanisms of more complicated ORR catalysts, however, have not been well-known yet. These complicated systems at least include the recent hot topics of efficient, durable and low-cost catalysts, such as "metal-free" heteroatom-doped carbons, carbon-transition metal hybrid, spinel/carbon hybrid and perovskite/carbon hybrid, etc. Another challenge comes from the further understanding of fundamental principles of the origin of ORR and identifying "hot spots" that are catalytically active for ORR. Some progress has been made on establishing the relationship between the electrocatalytic performance and the physical/chemical properties of catalysts, as stated in Section 2 and 3. Hitherto, more and more efficient ORR catalysts are developed by empirical fast-screening electrochemical techniques such as RDE and RRDE. It is highly desirable to find some universal performance descriptors that can be linked to the electrocatalytic activity measured experimentally. Some encouraging pioneer works had been reported for the precious metal-based and perovskite oxide-based catalysts.

The state-of-the-art catalysts have some shortcomings. Precious-metals are costly and scare, so that the large scale deployment for industrial applications seems luxury and not sustainable. The nonmetal-doped carbons and carbon-transition metal hybrids are not durable because of the carbon corrosion problem. Besides the insufficient ORR activity on par with the precious metal and nanocarbon catalysts, transition metal oxides are generally of poor electric conductivity and the incorporation of carbon additives suffer the same carbon corrosion problem. The pursuit of more efficient, more durable and less costly ORR catalysts will continue to be future challenges. Finally, more works should be carried out on applying those fast-screened ORR catalysts to practical devices based on oxygen electrocatalysis, such as metal-air batteries, fuel cells, microbial fuel cells, etc.

AUTHOR INFORMATION

Corresponding Authors

*E-mail: zl-liu@imre.a-star.edu.sg.
*E-mail: andyhor@imre.a-star.edu.sg.
*E-mail: y-zong@imre.a-star.edu.sg.

Funding

This research was supported by the Advanced Energy Storage Research Programme (Grants IMRE/12−2P0503 and IMRE/12−2P0504), Institute of Materials Research and Engineering (IMRE) of the Agency for Science, Technology and Research (A*STAR).

Notes

The authors declare no competing financial interest.

REFERENCES

(1) Cheng, F.; Chen, J. *Chem. Soc. Rev.* **2012**, *41*, 2172−2192.
(2) Lee, J.; Jeong, B.; Ocon, J. D. *Curr. Appl. Phys.* **2013**, *13*, 309−321.
(3) Adzic, R. R. in *Electrocatalysis*; Lipkowski, J., Ross, P. N., Eds.; Wiley-VCH: New York, 1998; p 197.
(4) Spendelow, J. S.; Wieckowski, A. *Phys. Chem. Chem. Phys.* **2007**, *9*, 2654−2675.
(5) Ramaswamy, N.; Mukerjee, S. *Adv. Phys. Chem.* **2012**, *2012*, Article no. 491604.
(6) Li, Y.; Dai, H. *Chem. Soc. Rev.* **2014**, *43*, 5257−5275.
(7) Pei, P.; Wang, K.; Ma, Z. *Appl. Energy* **2014**, *128*, 315−324.
(8) Neburchilov, V.; Wang, H.; Martin, J. J.; Qu, W. *J. Power Sources* **2010**, *195*, 1271−1291.
(9) Pan, J.; Chen, C.; Zhuang, L.; Lu, J. *Acc. Chem. Res.* **2012**, *45*, 473−481.

DOI: 10.1021/acscatal.5b00524
ACS Catal. 2015, 5, 4643−4667

(10) An, L.; Zhao, T. S.; Li, Y.; Wu, Q. *Energy Environ. Sci.* **2012**, *5*, 7536−7538.
(11) An, L.; Chai, Z. H.; Zeng, L.; Tan, P.; Zhao, T. S. *Int. J. Hydrogen Energy* **2013**, *38*, 14067−14075.
(12) Yu, E. H.; Krewer, U.; Scott, K. *Energies* **2010**, *3*, 1499−1528.
(13) Mohan, S. V.; Velvizhi, G.; Modestra, J. A.; Srikanth, S. *Renewable Sustainable Energy Rev.* **2014**, *40*, 779−797.
(14) Wang, H.; Park, J.-D.; Ren, Z. J. *Environ. Sci. Technol.* **2015**, *49*, 3267−3277.
(15) Gattrell, M.; MacDougall, B. In *Handbook of Fuel Cells: Fundamentals, Technology, and Applications*; Vielstich, W., Lamm, A., Gasteiger, H. A., Eds.; Wiley-VCH: New York, 2003; Vol. *2*, Part 5, pp 1−22.
(16) Greeley, J.; Markovic, N. M. *Energy Environ. Sci.* **2012**, *5*, 9246−9256.
(17) Tong, Y. J. *Chem. Soc. Rev.* **2012**, *41*, 8195−8209.
(18) Zinola, C. F.; Arvia, A. J.; Estiu, G. L.; Castro, E. A. *J. Phys. Chem.* **1994**, *98*, 7566−7576.
(19) Nie, Y.; Li, L.; Wei, Z. *Chem. Soc. Rev.* **2015**, *44*, 2168−2201.
(20) Quan, Z.; Wang, Y.; Fang, J. *Acc. Chem. Res.* **2012**, *46*, 191−202.
(21) Wang, C.; Markovic, N. M.; Stamenkovic, V. R. *ACS Catal.* **2012**, *2*, 891−898.
(22) Cao, M.; Wu, D.; Cao, R. *ChemCatChem* **2014**, *6*, 26−45.
(23) Hayden, B. E. *Acc. Chem. Res.* **2013**, *46*, 1858−1866.
(24) Koper, M. T. M. *Nanoscale* **2011**, *3*, 2054−2073.
(25) Guo, S.; Zhang, S.; Sun, S. *Angew. Chem., Int. Ed.* **2013**, *52*, 8526−8544.
(26) Long, N. V.; Thi, C. M.; Yong, Y.; Nogami, M.; Ohtaki, M. *J. Nanosci. Nanotechnol.* **2013**, *13*, 4799−4824.
(27) Shao, M. *J. Power Sources* **2011**, *196*, 2433−2444.
(28) Wu, G.; Zelenay, P. *Acc. Chem. Res.* **2013**, *46*, 1878−1889.
(29) Watanabe, M.; Tryk, D. A.; Wakisaka, M.; Yano, H.; Uchida, H. *Electrochim. Acta* **2012**, *84*, 187−201.
(30) Xu, Y.; Zhang, B. *Chem. Soc. Rev.* **2014**, *43*, 2439−2450.
(31) Liu, M.; Zhang, R.; Chen, W. *Chem. Rev.* **2014**, *114*, 5117−5160.
(32) Katsounaros, I.; Cherevko, S.; Zeradjanin, A. R.; Mayrhofer, K. J. J. *Angew. Chem., Int. Ed.* **2014**, *53*, 102−121.
(33) Anastasijević, N. A.; Vesović, V.; Adžić, R. R. *J. Electroanal. Chem. Interfacial Electrochem.* **1987**, *229*, 305−316.
(34) Anastasijević, N. A.; Vesović, V.; Adžić, R. R. *J. Electroanal. Chem. Interfacial Electrochem.* **1987**, *229*, 317−325.
(35) Yeager, E. *J. Mol. Catal.* **1986**, *38*, 5−25.
(36) Li, Q.; Cao, R.; Cho, J.; Wu, G. *Adv. Energy Mater.* **2014**, *4*, 1301415.
(37) Vanýsek, P. In *CNC Handbook of Chemistry and Physics*, 90th ed.; Lide, D. R, Eds.; CRC Press (Taylor and Francis Group): Boca Raton, FL, 2009; Section 8, p 23.
(38) Bard, A. J.; Faulkner, J. R. *Electrochemical Methods: Fundamental and Applications*, 2nd ed.; John Wiley & Sons: New York, 2001; p 341.
(39) Stefanova, V.; Dobrovolska, T.; Miletiev, R.; Georgiev, M.; Simeonov, I. *Bulg. Chem. Commun.* **2013**, *45*, 144−150.
(40) Ge, X. M.; Goh, F. W. T.; Li, B.; Hor, T. S. A.; Zhang, J.; Xiao, P.; Wang, X.; Zong, Y.; Liu, Z. L. *Nanoscale* **2015**, *7*, 9046−9054.
(41) Geniès, L.; Faure, R.; Durand, R. *Electrochim. Acta* **1998**, *44*, 1317−1327.
(42) Paulus, U. A.; Schmidt, T. J.; Gasteiger, H. A.; Behm, R. J. *J. Electroanal. Chem.* **2001**, *495*, 134−145.
(43) Tsai, Y. L.; Huang, K. L.; Yang, C. C.; Ye, J. S.; Pan, L. S.; Lee, C. L. *Int. J. Hydrogen Energy* **2014**, *39*, 5528−5536.
(44) Trasatti, S. In *Handbook of Fuel Cells: Fundamentals, Technology, and Applications*; Vielstich, W., Lamm, A., Gasteiger, H. A., Eds.; Wiley-VCH: New York, 2003; Vol. *2*, Part 2, pp 1−9.
(45) Bockris, J. O'M.; Reddy, A. K. N.; Gamboa-Aldeco, M. *Modern Electrochemistry 2A: Fundamentals of Electrodics*; Kluwer Academic Publishers: New York, 2002; p 1067.
(46) Hu, P.; Song, Y.; Chen, L.; Chen, S. *Nanoscale* **2015**, *7*, 9627−9636.
(47) Tarasevich, M. R.; Korchagin, O. V. *Russ. J. Electrochem.* **2013**, *49*, 600−618.
(48) Bockris, J. O'M.; Reddy, A. K. N.; Gamboa-Aldeco, M. *Modern Electrochemistry 1: Ionics*; Kluwer Academic Publishers: New York, 2002; p 230.
(49) Bockris, J. O'M.; Reddy, A. K. N.; Gamboa-Aldeco, M. *Modern Electrochemistry 2A: Fundamentals of Electrodics*; Kluwer Academic Publishers: New York, 2002; p 828.
(50) Kim, J.; Gewirth, A. A. *J. Phys. Chem. B* **2006**, *110*, 2565−2571.
(51) Luo, Y. R. In *CNC Handbook of Chemistry and Physics*, 90th ed.; Lide, D. R, Eds.; CRC Press (Taylor and Francis Group): Boca Raton, FL, 2009; Section 9, pp 66−68.
(52) Blizanac, B. B.; Ross, P. N.; Markovic, N. M. *Electrochim. Acta* **2007**, *52*, 2264−2271.
(53) Poux, T.; Bonnefont, A.; Ryabova, A.; Kerangueven, G.; Tsirlina, G. A.; Savinova, E. R. *Phys. Chem. Chem. Phys.* **2014**, *16*, 13595−13600.
(54) Shao, M. H.; Adzic, R. R. *J. Phys. Chem. B* **2005**, *109*, 16563−16566.
(55) Sepa, D. B.; Vojnovic, M. V.; Damjanovic, A. *Electrochim. Acta* **1980**, *25*, 1491−1496.
(56) Ross, P. N. Jr. In *Handbook of Fuel Cells: Fundamentals, Technology, and Applications*; Vielstich, W., Lamm, A., Gasteiger, H. A., Eds.; Wiley-VCH: New York, 2003; Vol. *2*, Chapter 31, p 465.
(57) Divišek, J.; Kastening, B. *J. Electroanal. Chem.* **1975**, *65*, 603−621.
(58) Yang, H. H.; McCreery, R. L. *J. Electrochem. Soc.* **2000**, *147*, 3420−3428.
(59) Genies, L.; Bultel, Y.; Faure, R.; Durand, R. *Electrochim. Acta* **2003**, *48*, 3879−3890.
(60) Wiggins-Camacho, J. D.; Stevenson, K. J. *J. Phys. Chem. C* **2011**, *115*, 20002−20010.
(61) Shao, M. H.; Liu, P.; Adzic, R. R. *J. Am. Chem. Soc.* **2006**, *128*, 7408−7409.
(62) Goodenough, J. B.; Cushing, B. L. In *Handbook of Fuel Cells: Fundamentals, Technology, and Applications*; Vielstich, W., Lamm, A., Gasteiger, H. A., Eds.; Wiley-VCH: New York, 2003; Vol. *2*, Part 5, pp 1−14.
(63) Matsumoto, Y.; Yoneyama, H.; Tamura, H. *J. Electroanal. Chem. Interfacial Electrochem.* **1977**, *79*, 319−326.
(64) Matsumoto, Y.; Yoneyama, H.; Tamura, H. *J. Electroanal. Chem. Interfacial Electrochem.* **1977**, *83*, 237−243.
(65) Suntivich, J.; Gasteiger, H. A.; Yabuuchi, N.; Nakanishi, H.; Goodenough, J. B.; Shao-Horn, Y. *Nat. Chem.* **2011**, *3*, 546−550.
(66) Mueller, D. N.; Machala, M. L.; Bluhm, H.; Chueh, W. C. asds. *Nat. Commun.* **2015**, *6*, Articleno. 6097.
(67) Wang, Y.; Balbuena, P. B. *J. Phys. Chem. B* **2005**, *109*, 18902−18906.
(68) Markovic, N.; Gasteiger, H.; Ross, P. N. *J. Electrochem. Soc.* **1997**, *144*, 1591−1597.
(69) Chen, A.; Holt-Hindle, P. *Chem. Rev.* **2010**, *110*, 3767−3804.
(70) Tammeveski, K.; Tenno, T.; Claret, J.; Ferrater, C. *Electrochim. Acta* **1997**, *42*, 893−897.
(71) Perez, J.; Gonzalez, E. R.; Ticianelli, E. A. *Electrochim. Acta* **1998**, *44*, 1329−1339.
(72) Jäger, R.; Härk, E.; Kasatkin, P. E.; Lust, E. *J. Electrochem. Soc.* **2014**, *161*, F861−F867.
(73) Härk, E.; Jäger, R.; Lust, E. *ECS Trans.* **2014**, *59*, 137−144.
(74) Härk, E.; Jäger, R.; Lust, E. *Electrocatalysis* **2015**, *6*, 242−254.
(75) Zhong, X.; Yu, H.; Wang, X.; Liu, L.; Jiang, Y.; Wang, L.; Zhuang, G.; Chu, Y.; Li, X.; Wang, J. G. *ACS Appl. Mater. Interfaces* **2014**, *6*, 13448−13454.
(76) Lee, C. L.; Yang, C. C.; Liu, C. R.; Liu, Z. T.; Ye, J. S. *J. Power Sources* **2014**, *268*, 712−717.
(77) Han, X.; Cheng, F.; Zhang, T.; Yang, J.; Hu, Y.; Chen, J. *Adv. Mater.* **2014**, *26*, 2047−2051.
(78) Zhao, S.; Wangstrom, A. E.; Liu, Y.; Rigdon, W. A.; Mustain, W. E. *Electrochim. Acta* **2015**, *157*, 175−182.

DOI: 10.1021/acscatal.5b00524
ACS Catal. 2015, 5, 4643−4667

(79) Adzic, R. R.; Strbac, S.; Anastasijevic, N. *Mater. Chem. Phys.* **1989**, *22*, 349−375.
(80) Markovic, N. M.; Adzic, R. R.; Cahan, B. D.; Yeager, E. B. *J. Electroanal. Chem.* **1994**, *377*, 249−259.
(81) Quaino, P.; Luque, N. B.; Nazmutdinov, R.; Santos, E.; Schmickler, W. *Angew. Chem., Int. Ed.* **2012**, *51*, 12997−13000.
(82) Prieto, A.; Hernández, J.; Herrero, E.; Feliu, J. *J. Solid State Electrochem.* **2003**, *7*, 599−606.
(83) Awad, M. I.; Ohsaka, T. *J. Power Sources* **2013**, *226*, 306−312.
(84) Xu, S.; Wu, P. *J. Mater. Chem. A* **2014**, *2*, 13682−13690.
(85) Guo, S.; Sun, S. *J. Am. Chem. Soc.* **2012**, *134*, 2492−2495.
(86) Govindhan, M.; Chen, A. *J. Power Sources* **2015**, *274*, 928−936.
(87) Yin, H.; Tang, H.; Wang, D.; Gao, Y.; Tang, Z. *ACS Nano* **2012**, *6*, 8288−8297.
(88) Kim, S.-S.; Kim, Y.-R.; Chung, T. D.; Sohn, B.-H. *Adv. Funct. Mater.* **2014**, *24*, 2764−2771.
(89) Song, Y.; Liu, K.; Chen, S. *Langmuir* **2012**, *28*, 17143−17152.
(90) Srejic, I.; Rakocevic, Z.; Nenadovic, M.; Strbac, S. *Electrochim. Acta* **2015**, *169*, 22−31.
(91) Lima, F. H. B.; Zhang, J.; Shao, M. H.; Sasaki, K.; Vukmirovic, M. B.; Ticianelli, E. A.; Adzic, R. R. *J. Phys. Chem. C* **2006**, *111*, 404−410.
(92) Erikson, H.; Sarapuu, A.; Alexeyeva, N.; Tammeveski, K.; Solla-Gullón, J.; Feliu, J. M. *Electrochim. Acta* **2012**, *59*, 329−335.
(93) Huang, K. L.; Liu, Z. T.; Lee, C. L. *Electrochim. Acta* **2015**, *157*, 78−87.
(94) Shao, M. H.; Huang, T.; Liu, P.; Zhang, J.; Sasaki, K.; Vukmirovic, M. B.; Adzic, R. R. *Langmuir* **2006**, *22*, 10409−10415.
(95) Xiao, L.; Zhuang, L.; Liu, Y.; Lu, J.; Abruña, H. D. *J. Am. Chem. Soc.* **2009**, *131*, 602−608.
(96) Poon, K. C.; Tan, D. C. L.; Vo, T. D. T.; Khezri, B.; Su, H.; Webster, R. D.; Sato, H. *J. Am. Chem. Soc.* **2014**, *136*, 5217−5220.
(97) Sarapuu, A.; Kasikov, A.; Wong, N.; Lucas, C. A.; Sedghi, G.; Nichols, R. J.; Tammeveski, K. *Electrochim. Acta* **2010**, *55*, 6768−6774.
(98) Jiang, L.; Hsu, A.; Chu, D.; Chen, R. *J. Electrochem. Soc.* **2009**, *156*, B643−B649.
(99) Jukk, K.; Alexeyeva, N.; Ritslaid, P.; Kozlova, J.; Sammelselg, V.; Tammeveski, K. *Electrocatalysis* **2013**, *4*, 42−48.
(100) Jukk, K.; Kongi, N.; Matisen, L.; Kallio, T.; Kontturi, K.; Tammeveski, K. *Electrochim. Acta* **2014**, *137*, 206−212.
(101) Huang, Y. X.; Xie, J. F.; Zhang, X.; Xiong, L.; Yu, H. Q. *ACS Appl. Mater. Interfaces* **2014**, *6*, 15795−15801.
(102) Lu, Y.; Jiang, Y.; Gao, X.; Wang, X.; Chen, W. *J. Am. Chem. Soc.* **2014**, *136*, 11687−11697.
(103) Yin, H.; Liu, S.; Zhang, C.; Bao, J.; Zheng, Y.; Han, M.; Dai, Z. *ACS Appl. Mater. Interfaces* **2014**, *6*, 2086−2094.
(104) Liu, S.; Zhang, Q.; Li, Y.; Han, M.; Gu, L.; Nan, C.; Bao, J.; Dai, Z. *J. Am. Chem. Soc.* **2015**, *137*, 2820−2823.
(105) Sekol, R. C.; Li, X.; Cohen, P.; Doubek, G.; Carmo, M.; Taylor, A. D. *Appl. Catal., B* **2013**, *138*−*139*, 285−293.
(106) Li, S. S.; Wang, A. J.; Hu, Y. Y.; Fang, K. M.; Chen, J. R.; Feng, J. J. *J. Mater. Chem. A* **2014**, *2*, 18177−18183.
(107) Chatenet, M.; Genies-Bultel, L.; Aurousseau, M.; Durand, R.; Andolfatto, F. *J. Appl. Electrochem.* **2002**, *32*, 1131−1140.
(108) Guo, J.; Hsu, A.; Chu, D.; Chen, R. *J. Phys. Chem. C* **2010**, *114*, 4324−4330.
(109) Yi, Q.; Niu, F.; Li, L.; Du, R.; Zhou, Z.; Liu, X. *J. Electroanal. Chem.* **2011**, *654*, 60−65.
(110) Liu, B.; Wang, M. *Russ. J. Electrochem.* **2014**, *50*, 476−481.
(111) Blizanac, B. B.; Ross, P. N.; Marković, N. M. *J. Phys. Chem. B* **2006**, *110*, 4735−4741.
(112) Singh, P.; Buttry, D. A. *J. Phys. Chem. C* **2012**, *116*, 10656−10663.
(113) Han, J. J.; Li, N.; Zhang, T. Y. *J. Power Sources* **2009**, *193*, 885−889.
(114) Wang, Q.; Cui, X.; Guan, W.; Zhang, L.; Fan, X.; Shi, Z.; Zheng, W. *J. Power Sources* **2014**, *269*, 152−157.
(115) Demarconnay, L.; Coutanceau, C.; Léger, J. M. *Electrochim. Acta* **2004**, *49*, 4513−4521.
(116) Fazil, A.; Chetty, R. *Electroanalysis* **2014**, *26*, 2380−2387.
(117) Lee, K.; Ahmed, M. S.; Jeon, S. *J. Electrochem. Soc.* **2015**, *162*, F1−F8.
(118) Jin, S.; Chen, M.; Dong, H.; He, B.; Lu, H.; Su, L.; Dai, W.; Zhang, Q.; Zhang, X. *J. Power Sources* **2015**, *274*, 1173−1179.
(119) Yuan, L.; Jiang, L.; Liu, J.; Xia, Z.; Wang, S.; Sun, G. *Electrochim. Acta* **2014**, *135*, 168−174.
(120) Wu, Q.; Jiang, L.; Qi, L.; Yuan, L.; Wang, E.; Sun, G. *Electrochim. Acta* **2014**, *123*, 167−175.
(121) Goh, F. W. T.; Liu, Z.; Ge, X.; Zong, Y.; Du, G.; Hor, T. S. A. *Electrochim. Acta* **2013**, *114*, 598−604.
(122) Gong, K.; Du, F.; Xia, Z.; Durstock, M.; Dai, L. *Science* **2009**, *323*, 760−764.
(123) Ikeda, T.; Boero, M.; Huang, S. F.; Terakura, K.; Oshima, M.; Ozaki, J. I. *J. Phys. Chem. C* **2008**, *112*, 14706−14709.
(124) Kaukonen, M.; Kujala, R.; Kauppinen, E. *J. Phys. Chem. C* **2011**, *116*, 632−636.
(125) Paraknowitsch, J. P.; Thomas, A. *Energy Environ. Sci.* **2013**, *6*, 2839−2855.
(126) Dai, L.; Xue, Y.; Qu, L.; Choi, H. J.; Baek, J. B. *Chem. Rev.* **2015**, *115*, 4823.
(127) Liang, H. W.; Wu, Z. Y.; Chen, L. F.; Li, C.; Yu, S. H. *Nano Energy* **2015**, *11*, 366−376.
(128) Wang, P.; Wang, Z.; Jia, L.; Xiao, Z. *Phys. Chem. Chem. Phys.* **2009**, *11*, 2730−2740.
(129) Luo, Z.; Lim, S.; Tian, Z.; Shang, J.; Lai, L.; MacDonald, B.; Fu, C.; Shen, Z.; Yu, T.; Lin, J. *J. Mater. Chem.* **2011**, *21*, 8038−8044.
(130) Maldonado, S.; Stevenson, K. J. *J. Phys. Chem. B* **2005**, *109*, 4707−4716.
(131) Wang, H.; Xie, M.; Thia, L.; Fisher, A.; Wang, X. *J. Phys. Chem. Lett.* **2013**, *5*, 119−125.
(132) Pachfule, P.; Dhavale, V. M.; Kandambeth, S.; Kurungot, S.; Banerjee, R. *Chem. - Eur. J.* **2013**, *19*, 974−980.
(133) Lai, L.; Potts, J. R.; Zhan, D.; Wang, L.; Poh, C. K.; Tang, C.; Gong, H.; Shen, Z.; Lin, J.; Ruoff, R. S. *Energy Environ. Sci.* **2012**, *5*, 7936−7942.
(134) Biddinger, E. J.; Ozkan, U. S. *J. Phys. Chem. C* **2010**, *114*, 15306−15314.
(135) Sharifi, T.; Hu, G.; Jia, X.; Wågberg, T. *ACS Nano* **2012**, *6*, 8904−8912.
(136) Zhang, B.; Wen, Z.; Ci, S.; Mao, S.; Chen, J.; He, Z. *ACS Appl. Mater. Interfaces* **2014**, *6*, 7464−7470.
(137) Matter, P. H.; Zhang, L.; Ozkan, U. S. *J. Catal.* **2006**, *239*, 83−96.
(138) Tuci, G.; Zafferoni, C.; D'Ambrosio, P.; Caporali, S.; Ceppatelli, M.; Rossin, A.; Tsoufis, T.; Innocenti, M.; Giambastiani, G. *ACS Catal.* **2013**, *3*, 2108−2111.
(139) Sidik, R. A.; Anderson, A. B.; Subramanian, N. P.; Kumaraguru, S. P.; Popov, B. N. *J. Phys. Chem. B* **2006**, *110*, 1787−1793.
(140) Tuci, G.; Zafferoni, C.; Rossin, A.; Milella, A.; Luconi, L.; Innocenti, M.; Truong Phuoc, L.; Duong-Viet, C.; Pham-Huu, C.; Giambastiani, G. *Chem. Mater.* **2014**, *26*, 3460−3470.
(141) Liu, M.; Song, Y.; He, S.; Tjiu, W. W.; Pan, J.; Xia, Y.-Y.; Liu, T. *ACS Appl. Mater. Interfaces* **2014**, *6*, 4214−4222.
(142) Bo, X.; Han, C.; Zhang, Y.; Guo, L. *ACS Appl. Mater. Interfaces* **2014**, *6*, 3023−3030.
(143) Cong, H. P.; Wang, P.; Gong, M.; Yu, S. H. *Nano Energy* **2014**, *3*, 55−63.
(144) Ratso, S.; Kruusenberg, I.; Vikkisk, M.; Joost, U.; Shulga, E.; Kink, I.; Kallio, T.; Tammeveski, K. *Carbon* **2014**, *73*, 361−370.
(145) Wang, Y.; Jiang, X. *ACS Appl. Mater. Interfaces* **2013**, *5*, 11597−11602.
(146) Pan, F.; Jin, J.; Fu, X.; Liu, Q.; Zhang, J. *ACS Appl. Mater. Interfaces* **2013**, *5*, 11108−11114.
(147) Nam, G.; Park, J.; Kim, S. T.; Shin, D. B.; Park, N.; Kim, Y.; Lee, J. S.; Cho, J. *Nano Lett.* **2014**, *14*, 1870−1876.
(148) Linden, D. L.; Reddy, T. B. *Handbook of Batteries*, 3rd ed.; McGraw-Hill: New York, 2002; Chapter 1, p 12.

DOI: 10.1021/acscatal.5b00524
ACS Catal. 2015, 5, 4643−4667

(149) Silva, R.; Voiry, D.; Chhowalla, M.; Asefa, T. *J. Am. Chem. Soc.* **2013**, *135*, 7823−7826.
(150) Wei, W.; Liang, H.; Parvez, K.; Zhuang, X.; Feng, X.; Müllen, K. *Angew. Chem.* **2014**, *126*, 1596−1600.
(151) Zhang, P.; Sun, F.; Xiang, Z.; Shen, Z.; Yun, J.; Cao, D. *Energy Environ. Sci.* **2014**, *7*, 442−450.
(152) Yang, L.; Jiang, S.; Zhao, Y.; Zhu, L.; Chen, S.; Wang, X.; Wu, Q.; Ma, J.; Ma, Y.; Hu, Z. *Angew. Chem., Int. Ed.* **2011**, *50*, 7132−7135.
(153) Wang, S.; Iyyamperumal, E.; Roy, A.; Xue, Y.; Yu, D.; Dai, L. *Angew. Chem., Int. Ed.* **2011**, *50*, 11756−11760.
(154) Wang, S.; Zhang, L.; Xia, Z.; Roy, A.; Chang, D. W.; Baek, J.-B.; Dai, L. *Angew. Chem., Int. Ed.* **2012**, *51*, 4209−4212.
(155) Liu, Y.; Chen, S.; Quan, X.; Yu, H.; Zhao, H.; Zhang, Y.; Chen, G. *J. Phys. Chem. C* **2013**, *117*, 14992−14998.
(156) Gong, Y. J.; Fei, H. L.; Zou, X. L.; Zhou, W.; Yang, S. B.; Ye, G. L.; Liu, Z.; Peng, Z. W.; Lou, J.; Vajtai, R.; Yakobson, B. I.; Tour, J. M.; Ajayan, P. M. *Chem. Mater.* **2015**, *27*, 1181−1186.
(157) Fei, H.; Ye, R.; Ye, G.; Gong, Y.; Peng, Z.; Fan, X.; Samuel, E. L. G.; Ajayan, P. M.; Tour, J. M. *ACS Nano* **2014**, *8*, 10837−10843.
(158) Zhao, Y.; Yang, L.; Chen, S.; Wang, X.; Ma, Y.; Wu, Q.; Jiang, Y.; Qian, W.; Hu, Z. *J. Am. Chem. Soc.* **2013**, *135*, 1201−1204.
(159) Yang, Z.; Yao, Z.; Li, G.; Fang, G.; Nie, H.; Liu, Z.; Zhou, X.; Chen, X. A.; Huang, S. *ACS Nano* **2011**, *6*, 205−211.
(160) Su, Y.; Zhang, Y.; Zhuang, X.; Li, S.; Wu, D.; Zhang, F.; Feng, X. *Carbon* **2013**, *62*, 296−301.
(161) Zhang, H.; Liu, X.; He, G.; Zhang, X.; Bao, S.; Hu, W. *J. Power Sources* **2015**, *279*, 252−258.
(162) Shi, Q.; Peng, F.; Liao, S.; Wang, H.; Yu, H.; Liu, Z.; Zhang, B.; Su, D. *J. Mater. Chem. A* **2013**, *1*, 14853−14857.
(163) Gao, S.; Liu, H.; Geng, K.; Wei, X. *Nano Energy* **2015**, *12*, 785−793.
(164) Liang, J.; Jiao, Y.; Jaroniec, M.; Qiao, S. Z. *Angew. Chem., Int. Ed.* **2012**, *51*, 11496−11500.
(165) Wu, J.; Jin, C.; Yang, Z.; Tian, J.; Yang, R. *Carbon* **2015**, *82*, 562−571.
(166) Gong, X.; Liu, S.; Ouyang, C.; Strasser, P.; Yang, R. *ACS Catal.* **2014**, *5*, 920−927.
(167) Zhao, S.; Liu, J.; Li, C.; Ji, W.; Yang, M.; Huang, H.; Liu, Y.; Kang, Z. *ACS Appl. Mater. Interfaces* **2014**, *6*, 22297−22304.
(168) Sun, X.; Zhang, Y.; Song, P.; Pan, J.; Zhuang, L.; Xu, W.; Xing, W. *ACS Catal.* **2013**, *3*, 1726−1729.
(169) Wang, L.; Ambrosi, A.; Pumera, M. *Angew. Chem., Int. Ed.* **2013**, *52*, 13818−13821.
(170) Yeager, E. *Electrochim. Acta* **1984**, *29*, 1527−1537.
(171) Gruenig, G.; Wiesener, K.; Gamburzev, S.; Iliev, I.; Kaisheva, A. *J. Electroanal. Chem. Interfacial Electrochem.* **1983**, *159*, 155−162.
(172) Scherson, D.; Tanaka, A. A.; Gupta, S. L.; Tryk, D.; Fierro, C.; Holze, R.; Yeager, E. B.; Lattimer, R. P. *Electrochim. Acta* **1986**, *31*, 1247−1258.
(173) Lalande, G.; Côté, R.; Guay, D.; Dodelet, J. P.; Weng, L. T.; Bertrand, P. *Electrochim. Acta* **1997**, *42*, 1379−1388.
(174) Wu, G.; Johnston, C. M.; Mack, N. H.; Artyushkova, K.; Ferrandon, M.; Nelson, M.; Lezama-Pacheco, J. S.; Conradson, S. D.; More, K. L.; Myers, D. J.; Zelenay, P. *J. Mater. Chem.* **2011**, *21*, 11392−11405.
(175) Lefèvre, M.; Proietti, E.; Jaouen, F.; Dodelet, J. P. *Science* **2009**, *324*, 71−74.
(176) Jaouen, F.; Proietti, E.; Lefevre, M.; Chenitz, R.; Dodelet, J. P.; Wu, G.; Chung, H. T.; Johnston, C. M.; Zelenay, P. *Energy Environ. Sci.* **2011**, *4*, 114−130.
(177) Wu, G.; More, K. L.; Johnston, C. M.; Zelenay, P. *Science* **2011**, *332*, 443−447.
(178) Zhao, S.; Yin, H.; Du, L.; He, L.; Zhao, K.; Chang, L.; Yin, G.; Zhao, H.; Liu, S.; Tang, Z. *ACS Nano* **2014**, *8*, 12660−12668.
(179) Liu, J.; Sun, X.; Song, P.; Zhang, Y.; Xing, W.; Xu, W. *Adv. Mater.* **2013**, *25*, 6879−6883.
(180) Song, P.; Zhang, Y.; Pan, J.; Zhuang, L.; Xu, W. *Chem. Commun.* **2015**, *51*, 1972−1975.
(181) Yan, X. H.; Xu, B. Q. *J. Mater. Chem. A* **2014**, *2*, 8617−8622.
(182) Lee, J. S.; Park, G. S.; Kim, S. T.; Liu, M.; Cho, J. *Angew. Chem., Int. Ed.* **2013**, *52*, 1026−1030.
(183) Lin, L.; Zhu, Q.; Xu, A. W. *J. Am. Chem. Soc.* **2014**, *136*, 11027−11033.
(184) Yang, W.; Liu, X.; Yue, X.; Jia, J.; Guo, S. *J. Am. Chem. Soc.* **2015**, *137*, 1436−1439.
(185) Gu, L.; Jiang, L.; Jin, J.; Liu, J.; Sun, G. *Carbon* **2015**, *82*, 572−578.
(186) Kim, B. J.; Lee, D. U.; Wu, J.; Higgins, D.; Yu, A.; Chen, Z. *J. Phys. Chem. C* **2013**, *117*, 26501−26508.
(187) Yin, H.; Zhang, C.; Liu, F.; Hou, Y. *Adv. Funct. Mater.* **2014**, *24*, 2930−2937.
(188) Yang, Z.; Wu, J.; Zheng, X.; Wang, Z.; Yang, R. *J. Power Sources* **2015**, *277*, 161−168.
(189) Jasinski, R. *Nature* **1964**, *201*, 1212−1213.
(190) Liang, H. W.; Wei, W.; Wu, Z. S.; Feng, X.; Müllen, K. *J. Am. Chem. Soc.* **2013**, *135*, 16002−16005.
(191) Wang, H.; Bo, X.; Wang, A.; Guo, L. *Electrochem. Commun.* **2013**, *36*, 75−79.
(192) Zheng, B.; Wang, J.; Wang, F. B.; Xia, X. H. *J. Mater. Chem. A* **2014**, *2*, 9079−9084.
(193) Trasatti, S. *Electrochim. Acta* **1984**, *29*, 1503−1512.
(194) Liang, Y.; Li, Y.; Wang, H.; Zhou, J.; Wang, J.; Regier, T.; Dai, H. *Nat. Mater.* **2011**, *10*, 780−786.
(195) Menezes, P. W.; Indra, A.; González-Flores, D.; Ranjbar Sahraie, N.; Zaharieva, I.; Schwarze, M.; Strasser, P.; Dau, H.; Driess, M. *ACS Catal.* **2015**, *5*, 2017.
(196) Zhang, G.; Li, C.; Liu, J.; Zhou, L.; Liu, R.; Han, X.; Huang, H.; Hu, H.; Liu, Y.; Kang, Z. *J. Mater. Chem. A* **2014**, *2*, 8184−8189.
(197) Wang, Q.; Yuan, H.; Feng, H.; Li, J.; Zhao, C.; Liu, J.; Qian, D.; Jiang, J.; Liu, Y. *RSC Adv.* **2014**, *4*, 18286−18293.
(198) Lee, E.; Jang, J. H.; Kwon, Y. U. *J. Power Sources* **2015**, *273*, 735−741.
(199) Ma, T. Y.; Zheng, Y.; Dai, S.; Jaroniec, M.; Qiao, S. Z. *J. Mater. Chem. A* **2014**, *2*, 8676−8682.
(200) Ge, X. M.; Liu, Y. Y.; Goh, F. W. T.; Hor, T. S. A.; Zong, Y.; Xiao, P.; Zhang, Z.; Lim, S. H.; Li, B.; Wang, X.; Liu, Z. L. *ACS Appl. Mater. Interfaces* **2014**, *6*, 12684−12691.
(201) Zhang, H.; Li, H.; Wang, H.; He, K.; Wang, S.; Tang, Y.; Chen, J. *J. Power Sources* **2015**, *280*, 640−648.
(202) Zhang, G.; Xia, B. Y.; Wang, X.; Lou, X. W. *Adv. Mater.* **2014**, *26*, 2408−2412.
(203) Zou, X.; Su, J.; Silva, R.; Goswami, A.; Sathe, B. R.; Asefa, T. *Chem. Commun.* **2013**, *49*, 7522−7524.
(204) Xiao, Y.; Hu, C.; Qu, L.; Hu, C.; Cao, M. *Chem. - Eur. J.* **2013**, *19*, 14271−14278.
(205) Cheng, F.; Shen, J.; Peng, B.; Pan, Y.; Tao, Z.; Chen, J. *Nat. Chem.* **2011**, *3*, 79−84.
(206) Zhu, H.; Zhang, S.; Huang, Y. X.; Wu, L.; Sun, S. *Nano Lett.* **2013**, *13*, 2947−2951.
(207) Ning, R.; Tian, J.; Asiri, A. M.; Qusti, A. H.; Al-Youbi, A. O.; Sun, X. *Langmuir* **2013**, *29*, 13146−13151.
(208) Mohanraju, K.; Sreejith, V.; Ananth, R.; Cindrella, L. *J. Power Sources* **2015**, *284*, 383−391.
(209) Singh, R. N.; Lal, B.; Malviya, M. *Electrochim. Acta* **2004**, *49*, 4605−4612.
(210) Barros, W. R. P.; Wei, Q.; Zhang, G.; Sun, S.; Lanza, M. R. V.; Tavares, A. C. *Electrochim. Acta* **2015**, *162*, 263−270.
(211) Su, Y.; Jiang, H.; Zhu, Y.; Yang, X.; Shen, J.; Zou, W.; Chen, J.; Li, C. *J. Mater. Chem. A* **2014**, *2*, 7281−7287.
(212) Wu, Z. S.; Yang, S.; Sun, Y.; Parvez, K.; Feng, X.; Muellen, K. *J. Am. Chem. Soc.* **2012**, *134*, 9082−9085.
(213) Liu, Y.; Wang, Y.; Xu, X.; Sun, P.; Chen, T. *RSC Adv.* **2014**, *4*, 4727−4731.
(214) Chowdhury, A. D.; Agnihotri, N.; Sen, P.; De, A. *Electrochim. Acta* **2014**, *118*, 81−87.
(215) Zhai, X.; Yang, W.; Li, M.; Lu, G.; Liu, J.; Zhang, X. *Carbon* **2013**, *65*, 277−286.

DOI: 10.1021/acscatal.5b00524
ACS Catal. 2015, 5, 4643−4667

(216) Liu, J.; Liu, J.; Song, W.; Wang, F.; Song, Y. *J. Mater. Chem. A* **2014**, *2*, 17477−17488.
(217) Gao, S.; Geng, K. *Nano Energy* **2014**, *6*, 44−50.
(218) Duan, J.; Chen, S.; Dai, S.; Qiao, S. Z. *Adv. Funct. Mater.* **2014**, *24*, 2072−2078.
(219) Duan, J.; Zheng, Y.; Chen, S.; Tang, Y.; Jaroniec, M.; Qiao, S. *Chem. Commun.* **2013**, *49*, 7705−7707.
(220) Xiao, J.; Chen, C.; Xi, J.; Xu, Y.; Xiao, F.; Wang, S.; Yang, S. *Nanoscale* **2015**, *7*, 7056−7064.
(221) Wang, C. H.; Yang, C. W.; Lin, Y. C.; Chang, S. T.; Chang, S. L. Y. *J. Power Sources* **2015**, *277*, 147−154.
(222) Hu, H.; Guan, B.; Xia, B.; Lou, X. W. *J. Am. Chem. Soc.* **2015**, *137*, 5590−5595.
(223) Wu, Z. Y.; Chen, P.; Wu, Q. S.; Yang, L. F.; Pan, Z.; Wang, Q. *Nano Energy* **2014**, *8*, 118−125.
(224) Ye, Y.; Kuai, L.; Geng, B. *J. Mater. Chem.* **2012**, *22*, 19132−19138.
(225) Qiao, L.; Xiao, H. Y.; Meyer, H. M.; Sun, J. N.; Rouleau, C. M.; Puretzky, A. A.; Geohegan, D. B.; Ivanov, I. N.; Yoon, M.; Weber, W. J.; Biegalski, M. D. *J. Mater. Chem. C* **2013**, *1*, 4628−4633.
(226) Liang, Y. Y.; Wang, H. L.; Diao, P.; Chang, W.; Hong, G. S.; Li, Y. G.; Gong, M.; Xie, L. M.; Zhou, J. G.; Wang, J.; Regier, T. Z.; Wei, F.; Dai, H. J. *J. Am. Chem. Soc.* **2012**, *134*, 15849−15857.
(227) Wang, M.; Huang, J.; Wang, M.; Zhang, D.; Zhang, W.; Li, W.; Chen, J. *Electrochem. Commun.* **2013**, *34*, 299−303.
(228) Wang, Y.; Cui, X.; Chen, L.; Wei, C.; Cui, F.; Yao, H.; Shi, J.; Li, Y. *Dalton Trans.* **2014**, *43*, 4163−4168.
(229) Wang, J.; Zhou, J.; Hu, Y.; Regier, T. *Energy Environ. Sci.* **2013**, *6*, 926−934.
(230) Xiao, J.; Kuang, Q.; Yang, S.; Xiao, F.; Wang, S.; Guo, L. *Sci. Rep.* **2013**, *3*, 2300.
(231) Bag, S.; Roy, K.; Gopinath, C. S.; Raj, C. R. *ACS Appl. Mater. Interfaces* **2014**, *6*, 2692−2699.
(232) Martin de Vidales, J. L.; Vila, E.; Rojas, R. M.; Garcia-Martinez, O. *Chem. Mater.* **1995**, *7*, 1716−1721.
(233) Liang, Y.; Wang, H.; Zhou, J.; Li, Y.; Wang, J.; Regier, T.; Dai, H. *J. Am. Chem. Soc.* **2012**, *134*, 3517−3523.
(234) de Vidales, J. L. M.; García-Martínez, O.; Vila, E.; Rojas, R. M.; Torralvo, M. J. *Mater. Res. Bull.* **1993**, *28*, 1135−1143.
(235) Nissinen, T.; Valo, T.; Gasik, M.; Rantanen, J.; Lampinen, M. *J. Power Sources* **2002**, *106*, 109−115.
(236) Nissinen, T. A.; Kiros, Y.; Gasik, M.; Leskelä, M. *Chem. Mater.* **2003**, *15*, 4974−4979.
(237) Das Sharma, A.; Mukhopadhyay, J.; Basu, R. N. *ECS Trans.* **2011**, *35*, 2509−2517.
(238) Liu, L.; Yang, Y. *Superlattices Microstruct.* **2013**, *54*, 26−38.
(239) El-Deab, M. S.; Ohsaka, T. *Angew. Chem., Int. Ed.* **2006**, *45*, 5963−5966.
(240) De Koninck, M.; Marsan, B. *Electrochim. Acta* **2008**, *53*, 7012−7021.
(241) Rios, E.; Gautier, J. L.; Poillerat, G.; Chartier, P. *Electrochim. Acta* **1998**, *44*, 1491−1497.
(242) Hu, L.; Wu, L.; Liao, M.; Hu, X.; Fang, X. *Adv. Funct. Mater.* **2012**, *22*, 998−1004.
(243) Liu, Z. Q.; Xu, Q. Z.; Wang, J. Y.; Li, N.; Guo, S. H.; Su, Y. Z.; Wang, H. J.; Zhang, J. H.; Chen, S. *Int. J. Hydrogen Energy* **2013**, *38*, 6657−6662.
(244) Kim, J.; Yin, X.; Tsao, K. C.; Fang, S.; Yang, H. *J. Am. Chem. Soc.* **2014**, *136*, 14646−14649.
(245) Risch, M.; Grimaud, A.; May, K. J.; Stoerzinger, K. A.; Chen, T. J.; Mansour, A. N.; Shao-Horn, Y. *J. Phys. Chem. C* **2013**, *117*, 8628−8635.
(246) Grimaud, A.; May, K. J.; Carlton, C. E.; Lee, Y. L.; Risch, M.; Hong, W. T.; Zhou, J.; Shao-Horn, Y. *Nat. Commun.* **2013**, *4*, 2439.
(247) Garcia, E. M.; Tarôco, H. A.; Matencio, T.; Domingues, R. Z.; dos Santos, J. A. F. *Int. J. Hydrogen Energy* **2012**, *37*, 6400−6406.
(248) Suntivich, J.; May, K. J.; Gasteiger, H. A.; Goodenough, J. B.; Shao-Horn, Y. *Science* **2011**, *334*, 1383−1385.
(249) Hong, W. T.; Risch, M.; Stoerzinger, K. A.; Grimaud, A.; Suntivich, J.; Shao-Horn, Y. *Energy Environ. Sci.* **2015**, *8*, 1404−1427.
(250) Risch, M.; Stoerzinger, K. A.; Maruyama, S.; Hong, W. T.; Takeuchi, I.; Shao-Horn, Y. *J. Am. Chem. Soc.* **2014**, *136*, 5229−5232.
(251) Jung, J. I.; Jeong, H. Y.; Lee, J. S.; Kim, M. G.; Cho, J. *Angew. Chem., Int. Ed.* **2014**, *53*, 4582−4586.
(252) Velraj, S.; Zhu, J. H. *J. Power Sources* **2013**, *227*, 48−52.
(253) Suntivich, J.; Perry, E.; Gasteiger, H.; Shao-Horn, Y. *Electrocatalysis* **2013**, *4*, 49−55.
(254) Hardin, W. G.; Slanac, D. A.; Wang, X.; Dai, S.; Johnston, K. P.; Stevenson, K. J. *J. Phys. Chem. Lett.* **2013**, *4*, 1254−1259.
(255) Malkhandi, S.; Yang, B.; Manohar, A. K.; Manivannan, A.; Prakash, G. K. S.; Narayanan, S. R. *J. Phys. Chem. Lett.* **2012**, *3*, 967−972.
(256) Chen, Z.; Yu, A.; Higgins, D.; Li, H.; Wang, H.; Chen, Z. *Nano Lett.* **2012**, *12*, 1946−1952.
(257) Matumoto, Y.; Yoneyama, H.; Tamura, H. *Chem. Lett.* **1975**, *4*, 661−662.
(258) Matsumoto, Y.; Yoneyama, H.; Tamura, H. *J. Electroanal. Chem. Interfacial Electrochem.* **1977**, *80*, 115−121.
(259) Bockris, J. O. M.; Otagawa, T. *J. Electrochem. Soc.* **1984**, *131*, 290−302.
(260) Hyodo, T.; Hayashi, M.; Miura, N.; Yamazoe, N. *J. Electrochem. Soc.* **1996**, *143*, L266−L267.
(261) Hyodo, T.; Hayashi, M.; Mitsutake, S.; Miura, N.; Yamazoe, N. *J. Appl. Electrochem.* **1997**, *27*, 745−745.
(262) Sunarso, J.; Torriero, A. A. J.; Zhou, W.; Howlett, P. C.; Forsyth, M. *J. Phys. Chem. C* **2012**, *116*, 5827−5834.
(263) Hu, J.; Wang, L.; Shi, L.; Huang, H. *J. Power Sources* **2014**, *269*, 144−151.
(264) Stoerzinger, K. A.; Lü, W.; Li, C.; Ariando; Venkatesan, T.; Shao-Horn, Y. *J. Phys. Chem. Lett.* **2015**, *6*, 1435−1440.
(265) Suntivich, J.; Gasteiger, H. A.; Yabuuchi, N.; Shao-Horn, Y. *J. Electrochem. Soc.* **2010**, *157*, B1263−B1268.
(266) Ono, K.; Kinumoto, T.; Tsumura, T.; Toyoda, M. *ECS Trans.* **2015**, *64*, 29−39.
(267) Kéranguéven, G.; Royer, S.; Savinova, E. *Electrochem. Commun.* **2015**, *50*, 28−31.
(268) Poux, T.; Bonnefont, A.; Kéranguéven, G.; Tsirlina, G. A.; Savinova, E. R. *ChemPhysChem* **2014**, *15*, 2108−2120.
(269) Li, X.; Qu, W.; Zhang, J.; Wang, H. *J. Electrochem. Soc.* **2011**, *158*, A597−A604.
(270) Fabbri, E.; Mohamed, R.; Levecque, P.; Conrad, O.; Koetz, R.; Schmidt, T. J. *ChemElectroChem* **2014**, *1*, 338−342.
(271) Fabbri, E.; Mohamed, R.; Levecque, P.; Conrad, O.; Kötz, R.; Schmidt, T. J. *ACS Catal.* **2014**, *4*, 1061−1070.
(272) Hermann, V.; Dutriat, D.; Müller, S.; Comninellis, C. *Electrochim. Acta* **2000**, *46*, 365−372.
(273) Hu, J.; Wang, L.; Shi, L.; Huang, H. *Electrochim. Acta* **2015**, *161*, 115−123.
(274) Liu, J.; Jiang, L.; Zhang, B.; Jin, J.; Su, D. S.; Wang, S.; Sun, G. *ACS Catal.* **2014**, *4*, 2998−3001.
(275) Liu, J.; Jiang, L.; Tang, Q.; Wang, E.; Qi, L.; Wang, S.; Sun, G. *Appl. Catal., B* **2014**, *148*, 212−220.
(276) Chaikittisilp, W.; Torad, N. L.; Li, C.; Imura, M.; Suzuki, N.; Ishihara, S.; Ariga, K.; Yamauchi, Y. *Chem. - Eur. J.* **2014**, *20*, 4217−4221.
(277) Linden, D. L.; Reddy, T. B. *Handbook of Batteries*, 3rd ed.; McGraw-Hill: New York, 2002; Chapter 10, p 1−32.
(278) Mao, L.; Zhang, D.; Sotomura, T.; Nakatsu, K.; Koshiba, N.; Ohsaka, T. *Electrochim. Acta* **2003**, *48*, 1015−1021.
(279) Cheng, F.; Su, Y.; Liang, J.; Tao, Z.; Chen, J. *Chem. Mater.* **2009**, *22*, 898−905.
(280) Cao, Y. L.; Yang, H. X.; Ai, X. P.; Xiao, L. F. *J. Electroanal. Chem.* **2003**, *557*, 127−134.
(281) Li, P. C.; Hu, C. C.; Lee, T. C.; Chang, W. S.; Wang, T. H. *J. Power Sources* **2014**, *269*, 88−97.
(282) Wei, C.; Yu, L.; Cui, C.; Lin, J.; Wei, C.; Mathews, N.; Huo, F.; Sritharan, T.; Xu, Z. *Chem. Commun.* **2014**, *50*, 7885−7888.

DOI: 10.1021/acscatal.5b00524
ACS Catal. 2015, 5, 4643−4667

(283) Zhang, J.; Guo, C.; Zhang, L.; Li, C. M. *Chem. Commun.* **2013**, *49*, 6334−6336.
(284) Lee, T.; Jeon, E. K.; Kim, B. S. *J. Mater. Chem. A* **2014**, *2*, 6167−6173.
(285) Chen, R.; Yan, J.; Liu, Y.; Li, J. *J. Phys. Chem. C* **2015**, *119*, 8032−8037.
(286) Bocchetta, P.; Gianoncelli, A.; Abyaneh, M. K.; Kiskinova, M.; Amati, M.; Gregoratti, L.; Jezersek, D.; Mele, C.; Bozzini, B. *Electrochim. Acta* **2014**, *137*, 535−545.
(287) Chen, R.; Li, H.; Chu, D.; Wang, G. *J. Phys. Chem. C* **2009**, *113*, 20689−20697.
(288) Lin, L.; Li, M.; Jiang, L.; Li, Y.; Liu, D.; He, X.; Cui, L. *J. Power Sources* **2014**, *268*, 269−278.
(289) Tang, H.; Yin, H.; Wang, J.; Yang, N.; Wang, D.; Tang, Z. *Angew. Chem., Int. Ed.* **2013**, *52*, 5585−5589.
(290) Schechter, A.; Stanevsky, M.; Mahammed, A.; Gross, Z. *Inorg. Chem.* **2012**, *51*, 22−24.
(291) Parimi, N. S.; Umasankar, Y.; Atanassov, P.; Ramasamy, R. P. *ACS Catal.* **2011**, *2*, 38−44.
(292) Khomenko, V. G.; Barsukov, V. Z.; Katashinskii, A. S. *Electrochim. Acta* **2005**, *50*, 1675−1683.
(293) Liao, L.; Bian, X.; Xiao, J.; Liu, B.; Scanlon, M. D.; Girault, H. H. *Phys. Chem. Chem. Phys.* **2014**, *16*, 10088−10094.
(294) Jin, Z.; Li, P.; Xiao, D. *Sci. Rep.* **2014**, *4*, 6712.
(295) Huang, T.; Mao, S.; Zhou, G.; Wen, Z.; Huang, X.; Ci, S.; Chen, J. *Nanoscale* **2014**, *6*, 9608−9613.
(296) Youn, D. H.; Bae, G.; Han, S.; Kim, J. Y.; Jang, J. W.; Park, H.; Choi, S. H.; Lee, J. S. *J. Mater. Chem. A* **2013**, *1*, 8007−8015.
(297) Lyalin, A.; Nakayama, A.; Uosaki, K.; Taketsugu, T. *J. Phys. Chem. C* **2013**, *117*, 21359−21370.
(298) Huang, T.; Mao, S.; Pu, H.; Wen, Z.; Huang, X.; Ci, S.; Chen, J. *J. Mater. Chem. A* **2013**, *1*, 13404−13410.
(299) Zhang, L. F.; Zhang, C. Y. *Nanoscale* **2014**, *6*, 1782−1789.
(300) Huo, R.; Jiang, W. J.; Xu, S.; Zhang, F.; Hu, J. S. *Nanoscale* **2014**, *6*, 203−206.
(301) Wu, Q.; Jiang, L.; Tang, Q.; Liu, J.; Wang, S.; Sun, G. *Electrochim. Acta* **2013**, *91*, 314−322.

DOI: 10.1021/acscatal.5b00524
ACS Catal. 2015, 5, 4643−4667